

Doctoral Dissertations and Master's Theses

Fall 2024

Adaptive Control and Estimation of the Center of Mass of a 5-degree-of-freedom Spacecraft Testbed

Pol Fontdegloria Balaguer
Embry-Riddle Aeronautical University, fontdegp@my.erau.edu

Follow this and additional works at: <https://commons.erau.edu/edt>



Part of the [Navigation, Guidance, Control and Dynamics Commons](#)

Scholarly Commons Citation

Fontdegloria Balaguer, Pol, "Adaptive Control and Estimation of the Center of Mass of a 5-degree-of-freedom Spacecraft Testbed" (2024). *Doctoral Dissertations and Master's Theses*. 858.
<https://commons.erau.edu/edt/858>

This Thesis - Open Access is brought to you for free and open access by Scholarly Commons. It has been accepted for inclusion in Doctoral Dissertations and Master's Theses by an authorized administrator of Scholarly Commons. For more information, please contact commons@erau.edu.

ADAPTIVE CONTROL AND ESTIMATION OF THE CENTER OF MASS
OF A 5-DEGREE-OF-FREEDOM SPACECRAFT TESTBED

By

Pol Fontdegloria Balaguer

A Thesis Submitted to the Faculty of Embry-Riddle Aeronautical University
In Partial Fulfillment of the Requirements for the Degree of
Master of Science in Aerospace Engineering

December 2024

Embry-Riddle Aeronautical University

Daytona Beach, Florida

To my parents and grandmother, gracies.

ACKNOWLEDGMENTS

To begin with, I would like to thank my advisor, Dr. Riccardo Bevilacqua. For his mentorship, encouragement, dedication, and guidance; and without whom this work would not have been possible. I would also like to thank the members of my committee, Dr. K. Merve Dogan, Dr. Dongeun Seo, and Dr. Richard Prazenica, who not only have been willing to partake on this research, but have also provided critical knowledge and advice throughout this process.

I would also like to acknowledge my fellow researchers from the ADAMUS Laboratory at Embry-Riddle Aeronautical University, for supporting my work and providing guidance at every step of this journey.

Finally, I would like to thank my parents for their unconditional support, which has allowed me to become who I am today. Thank you for pushing me to become a better person, thank you for prioritizing my future over your own needs, and thank you for being the way you are.

ABSTRACT

In space applications, on-ground experimentation is an essential step in control algorithm validation before real mission application. However, on-ground conditions greatly differ from space ones, where satellites operate under extremely low gravity and friction conditions. A common way to simulate these conditions is with air-bearing-based testbeds. These testbeds reduce friction significantly to almost space-like conditions. Air-bearing technology can provide virtually frictionless translational and rotational motion. However, when frictionless rotational motion is achieved, the testbed becomes highly sensible gravity torque. This external torque is produced by the offset between the predetermined geometrical center of rotation (*CoR*) and the center of mass (*CoM*) of the testbed, which makes the system behave like a three-dimensional pendulum.

Testbeds with rotational degrees of freedom must be designed to minimize this offset. However, manufacturing and assembly precision is limited, usually leading to a residual gravity torque that needs to be compensated for to obtain space-like conditions. The testbeds are designed to include sliding masses in the assembly, usually as stepper motors that can be commanded to a desired position to compensate the *CoM* to *CoR* offset. However, this offset is usually unknown, requiring an estimation process before offset compensation.

The literature shows various methods that can be used to estimate the unknown offset, such as batch estimation methods, filtering techniques, and active control techniques. However, all these methods present either one of the following problems. On the one hand, methods that allow the estimate of all three components of the offset vector at the same time require the use of actuators such as thrusters or momentum exchange devices. On the other hand, those methods that utilize the sliding masses as the only source of control input lead to an under-actuated system and fail to estimate all three components of the offset vector.

This work presents a novel reference model adaptive estimation and control law that ensures the estimation of all three components of the offset vector while taking into consideration a time-varying moment of inertia of a 5-degree-of-freedom (*DOF*) testbed. A

reference model is designed to obtain a control law that ensures the control input can be obtained from moving mass control (*MMC*) only.

The controller and estimation laws are demonstrated to produce asymptotic convergence of the error between system and desired states and asymptotic convergence of the estimation error to zero. Lyapunov stability theory concludes that the system's desired equilibrium point is stable, and Barbalat's Lemma is utilized to extend the conclusion to the asymptotic stability of the desired equilibrium point.

The control is validated in a numerical simulation environment using a Runge-Kutta fourth-order integrator. The results display asymptotic stability of the system states and estimation errors, validating the results obtained in the stability proof.

TABLE OF CONTENTS

ACKNOWLEDGMENTS	i
ABSTRACT	ii
LIST OF FIGURES	vii
NOMENCLATURE	viii
1 Introduction	1
1.1 Problem Statement	2
1.2 Research Goals	2
1.3 Importance of Research	3
2 Prior State of Knowledge & Preliminary Theory	4
2.1 Prior State of Knowledge	4
2.1.1 Batch Estimation Techniques	4
2.1.2 Kalman Filtering Methods	6
2.1.3 Active Control Techniques	7
2.2 Preliminary Theory	8
2.2.1 Quaternions	8
2.2.2 Model Reference Adaptive Control	11
2.2.3 Relevant Mathematical Operations	11
2.2.4 Lyapunov Stability	13
2.2.5 Barbalat's Lemma	14
3 Methodology	17
3.1 Dynamics Formulation	17
3.1.1 Testbed Dynamics	17
3.1.2 Moment of Inertia of the Testbed	18

3.1.3	External Torques acting on the Testbed	20
3.1.4	Desired Dynamics	22
3.1.5	Error Dynamics	24
3.2	Adaptive Estimation & Control Design	25
3.2.1	Lyapunov Stability	26
3.2.2	Barbalat's Lemma for Asymptotic Stability Extension	30
3.3	Parameter Convergence	32
3.4	Sliding Mass Control	36
4	Numerical Simulations	38
5	Results & Discussion	40
5.1	Desired Trajectory Results	40
5.2	Controlled System Results	41
5.3	Estimation Results	46
5.4	Sliding Mass Position Results	49
6	Conclusions & Future Work	50
REFERENCES		52

LIST OF FIGURES

Figure	Page
1.1 Schematic of the design of a 5- <i>DOF</i> testbed, with sliding masses m_1 , m_2 , and m_3 .	2
2.1 Xu et al. satellite attitude and dynamics simulator.[1]	5
2.2 SRL satellite attitude and dynamics simulator.[2]	6
3.1 <i>MoI</i> schematic for the derivation of the different contributing components.	19
3.2 Schematic of I and B frames, with gravity vector acting on the offset <i>CoM</i> .	21
3.3 Visualization of stabilized B frame with respect to I frame before T_1 .	34
3.4 Visualization of stabilized B frame with respect to I frame after T_2 .	35
5.1 Simulation results for angular rates of the D frame with respect to the I frame in the I frame $\vec{\omega}_{D/I}^I$ as a function of time.	40
5.2 Simulation results for the attitude of the D frame with respect to the I frame $\hat{q}_{I \rightarrow D}$ as a function of time.	41
5.3 Simulation results for angular rates of the B frame with respect to the D frame in the B frame $\vec{\omega}_{B/D}^B$ as a function of time.	42
5.4 Simulation results for angular rates of the B frame with respect to the D frame in the B frame $\vec{\omega}_{B/D}^B$ as a function of time, close up from 0 to 50 seconds.	42
5.5 Simulation results for angular rates of the B frame with respect to the D frame in the B frame $\vec{\omega}_{B/D}^B$ as a function of time, close up from 80 to 300 seconds.	43
5.6 Simulation results for the attitude of the B frame with respect to the D frame $\hat{q}_{D \rightarrow B}$ as a function of time.	44
5.7 Simulation results for the attitude of the B frame with respect to the D frame $\hat{q}_{D \rightarrow B}$ as a function of time, close up from 0 to 30 seconds.	45

5.8	Simulation results for the attitude of the B frame with respect to the D frame $\hat{q}_{D \rightarrow B}$ as a function of time, , close up from 50 to 200 seconds.	45
5.9	Simulation results for angular rates of the B frame with respect to the I frame in the B frame $\vec{\omega}_{B/I}^B$ as a function of time.	46
5.10	Simulation results for angular rates of the B frame with respect to the I frame in the I frame $\vec{\omega}_{B/I}^I$ as a function of time.	47
5.11	Simulation results for the attitude of the B frame with respect to the I frame $\hat{q}_{I \rightarrow B}$ as a function of time.	47
5.12	Simulation results for estimation errors $\tilde{\Theta}$ as a function of time.	48
5.13	Simulation results for estimation errors $\tilde{\Theta}$ as a function of time, close up from 0 to 30 seconds.	48
5.14	Simulation results commanded positions of the sliding masses $\vec{\sigma}$ as a function of time.	49

NOMENCLATURE

CAD Computer Aided Design

CLM Classical Levenberg-Marquardt

CoM Center of Mass

CoR Center of Rotation

DOF Degrees of Freedom

EKF Extended Kalman Filter

GD Gradient Descent

GNA Gauss-Newton Algorithm

IC Initial Conditions

KF Kalman Filter

LEO Low Earth Orbit

LSM Least Squares Method

MBS Mass Balancing System

MIMO Multi-Input Multi-Output

MMC Moving Mass Control

MoI Moment of Inertia

MRAC Model Reference Adaptive Control

UKF Unscented Kalman Filter

1 Introduction

Control algorithms are traditionally designed under the assumption of the system's known plant properties. However, it is not uncommon for the mass properties of satellites to deviate from the expected values. These fluctuations can occur due to various reasons, such as manufacturing and assembly inaccuracies, slight shifting of components during launch, or propellant usage. Unknown mass properties can lead to inaccuracies in dynamics modeling, which serves as the basis for the controller design and ultimately leads to the failure of the controlled system. Some of the error sources can be mitigated during the design and assembly phase. However, although a tight tolerance in manufacturing and assembly can reduce the uncertainty on the satellite's mass properties, there is a high increase in cost associated with it. Furthermore, there will always be uncontrollable factors that will lead to errors.

On-ground experimentation and testing of spacecraft control algorithms is critical for mission cost reduction and risk mitigation. Throughout the years, academic institutions have been developing testing platforms that allow researchers to verify their work and ensure correct operation on real hardware before a mission. One of the most common testing platforms is air-bearing-based testbeds, allowing virtually frictionless motion. These testbeds are used in different setups and are categorized depending on their allowed motion. Air-bearing technology allows for frictionless translational and rotational motion, up to six degrees of freedom [3]. Translational motion is obtained with flat air bearings, which mate with a precisely calibrated flat and smooth surface. Rotational motion is accomplished with spherical air bearings mounted to the structure, which supports the translational motion, onto where the top section of the testbed is mounted. The top subassembly of the testbed must have a precisely machined spherical artifact mounted, which directly interacts with the spherical air bearing, providing frictionless motion. The third axis of translational motion can also be achieved for a full six-degree-of-freedom, as presented by Saulnier et al. in [3]. When working with spacecraft testbeds with more than one rotational degree of freedom, gravity

torque becomes a disturbance that must be compensated if one is to simulate space-like conditions.

Gravity torque is generated by an offset between the *CoM* and *CoR*. When discussing testbeds with air-bearing technology, the *CoR* is determined by the geometrical center of the spherical bearing to which the artifact is mounted.

1.1 Problem Statement

Given a 5-*DOF* spacecraft testbed, with unknown *CoM*, this research aims to estimate the offset between *CoM* and *CoR*. The unknown vector can be visualized in Figure 1.1. The ultimate goal is to generate control and estimation laws based on model reference adaptive control theory and Lyapunov-based stability to estimate the *CoM* position and compensate for the offset by aligning it with the *CoR* position, reducing the effects of gravity torque acting on the testbed. This is to be achieved using the sliding masses shown in Figure 1.1 as the only control input, also known as moving mass control (*MMC*).

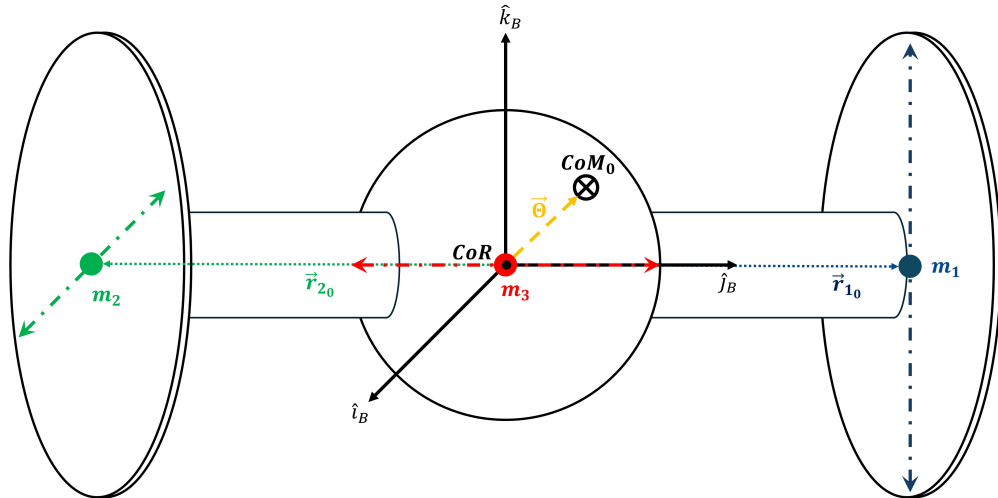


Figure 1.1 Schematic of the design of a 5-*DOF* testbed, with sliding masses m_1 , m_2 , and m_3 .

1.2 Research Goals

This research aims to provide a Model Reference Adaptive Control (*MRAC*) algorithm that allows estimation of an unknown *CoM* while maintaining attitude control of a 5-*DOF*

testbed. Furthermore, it aims to achieve the control objective by utilizing the gravity torque disturbance as the only control input for the testbed. This work also aims to obtain a complete estimation of the unknowns utilizing a single-control method approach. Finally, this work wants to account for time-varying moments of inertia due to the movement of the sliding masses.

1.3 Importance of Research

This research will allow simplification of the estimation process while ensuring accuracy and precision. This work will also reduce the number of processes required to estimate all three *CoM* offset axes with a single adaptive control law, improving the previous state-of-the-art requirements of a two-process approach. Furthermore, this research will be applied in the future to a 5-*DOF* testbed, which will ultimately allow replication of space-like conditions and improve spacecraft testing capabilities at Embry-Riddle Aeronautical University.

2 Prior State of Knowledge & Preliminary Theory

This chapter introduces the state of knowledge prior to the work presented in this document. **Section 2.1** emphasizes the literature relevant to this research while presenting other methods that have not been utilized in this work but are still required to understand the approach. Furthermore, the theory and concepts utilized as a basis for this work are presented in **Section 2.2**.

2.1 Prior State of Knowledge

Multiple methods and approaches can be found in the literature, which have been used to estimate unknown parameters of a system. This section focuses on the estimation methods that have been specifically utilized to solve the problem of *CoM* to *CoR* offset error for experimental testbeds with three rotational degrees of freedom. These techniques can be divided into three different categories:[4] Batch Estimation Techniques, Kalman Filtering (*KF*) Methods, and Active Control Techniques; presented in **Section 2.1.1**, **Section 2.1.2**, and **Section 2.1.3** respectively.

2.1.1 Batch Estimation Techniques

These techniques are based on off-line analysis of the testbed states to estimate the *CoM* to *CoR* offset. To guarantee the accuracy of the estimation, batch estimation techniques usually require an iterative process of the estimation and correction cycles.

Least Squares Method (*LSM*) is one of the batch estimation techniques reported in the literature in [5]. This technique benefits from the fact that it uses large data sets to estimate the *CoM* offset, which makes the system less susceptible to errors by oversampling the estimation equation and minimizing the mean squared error. de Silva et al. reported in [5] a minimum of 500 measurements required for the estimation of the offset. However, this large measurement requirement demands a high computational capacity. Furthermore, *LSM* is highly dependent on modeling errors, and it requires differentiation of the signal, which contributes to a higher level of sensor noise sensibility.

An improvement on this method is presented by Xu et al. in [1], which uses Recursive *LSM*, *LSM* with tracking differentiators, and extended tracking differentiators. Recursive *LSM* benefits from using an integration form for the estimation of parameters rather than the noise sensible differentiation form. However, this method has only been shown to work for a testbed with the use of reaction wheels to obtain the parameter estimation as shown by the testbed being used in [1] in Figure 2.1.

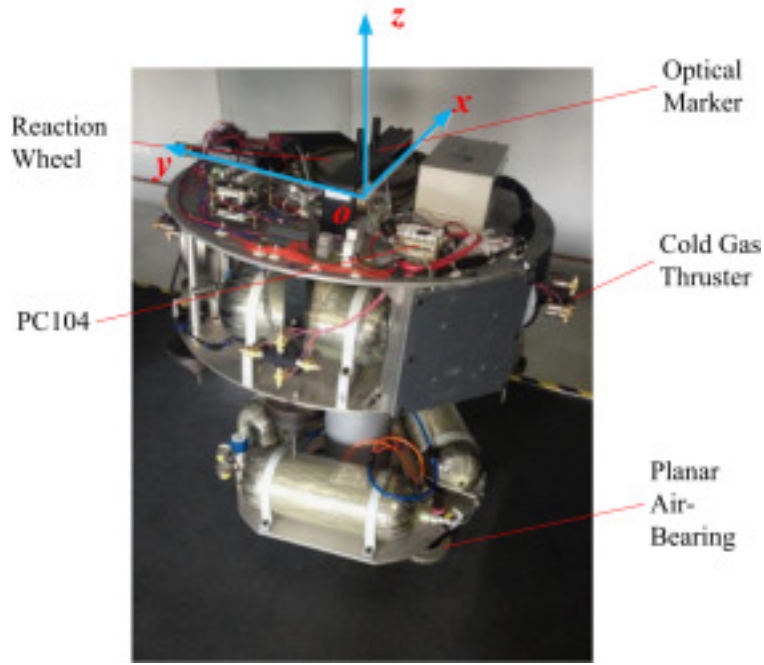


Figure 2.1 Xu et al. satellite attitude and dynamics simulator.[1]

Another method used for estimation of the *CoM* is the Classical Levenberg-Marquardt (*CLM*) estimation [6]. This method improves the results of *LSM* by determining the minimum of a multivariate function where the cost function is explained as the sum of squares error of the real and expected data. [2] This method is a combination of the Gauss-Newton algorithm (*GNA*) and gradient descent (*GD*), using the first algorithm when the parameters are close to their optimal value, and the second algorithm when far. This method is applied on a mass balancing system (*MBS*) by Sharifi et al. in [2], reducing the gravity torque to a value under 0.01 Nm. However, this work also requires the use of momentum exchange devices, as seen in Figure 2.2, which can easily increase the cost of the testbed.

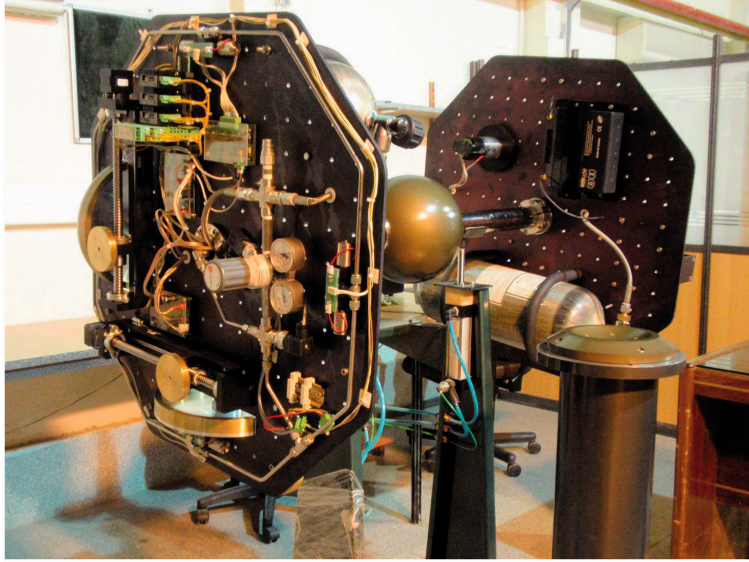


Figure 2.2 SRL satellite attitude and dynamics simulator.[2]

This work aims to achieve the control objective using only *MMC*, therefore improving on the proposed batch estimation methods above.

2.1.2 Kalman Filtering Methods

Filtering methods are the most commonly used approach to estimate *CoM* to *CoR* offset, and in general, reduce the computational cost of the procedure while reducing sensor noise sensibility. These include the traditional *KF*, as well as its variations in the Extended *KF* (*EKF*) and Unscented *KF* (*UKF*).

The traditional *KF* requires linearization of the highly non-linear system, which does not work well when the conditions assumed in the model simplification do not translate to the real system [7]. To avoid the condition of linearization required in the traditional *KF*, da Silva presents the application of *EKF* and *UKF*. The results presented by da Silva in [7] show that the *EKF* can provide better accuracy of the estimates as it considers the full plant model. However, the computation of a *EKF* method requires complex computation of the Jacobians while still displaying erratic behavior when high angular velocities are present in the system [7].

On the other hand, the *UKF* is based on approximating the probability distribution

instead of using the arbitrary nonlinear dynamics of the system. This method has advantages over the *EKF* of not having to calculate the complex Jacobian matrices and added robustness. Once again, the problem presented for these methods is the required momentum exchange devices, which are not to be used for the purposes of this work.

2.1.3 Active Control Techniques

Active control techniques are another alternative to estimate the *CoM* to *CoR*. Depending on the actuators used for the estimation and balancing maneuver, one can divide the approach into two subsections: fully actuated and under-actuated. Fully actuated active control techniques are demonstrated in [1, 8]. However, as for the filtering methods, the fully actuated approach requires heavy and expensive moment exchange devices. This study focuses on the under-actuated approach, using only the sliding masses to achieve the control objective: excite the testbed, estimate the *CoM* to *CoR* offset, and compensate for it. The main research on the under-actuated approach found in the literature is presented in [9]. Nonetheless, other authors have tackled this same approach in [10–12]. Chesi et al. present an under-actuated active control scheme that consists of two separate maneuvers in [9].

The first maneuver consists of an adaptive control scheme for transversal balancing, which compensates two of the three axes of the offset vector by attempting to bring angular rates orthogonal to the gravity vector to zero. Under the assumption that after the planar compensation, the testbed’s *CoM* to *CoR* offset vector is aligned with one of the body axes, Chesi et al. utilize a second *EKF*-based control maneuver to estimate the magnitude of the vertical imbalance vector.

However, the assumption that after the first maneuver, the testbed’s offset vector will be aligned with one of the body-fixed axes does not hold for all cases. It has been found that if the angular rates about the perpendicular plane to the gravity vector converge to zero before the estimation of the offset vector is performed, the testbed will not necessarily be aligned in its z-axis with the gravity vector. Furthermore, the convergence proof was performed using LaSalle’s Invariance Principle, which can only be used for autonomous systems [13].

Furthermore, the use of two separate maneuvers is not ideal in terms of time efficiency in a fast-paced testing environment. This thesis focuses on the improvement of the approach presented in [9] by providing an adaptive control law that allows for the estimation and compensation of all three components of the *CoM* to *CoR* offset with a single adaptive control and estimation law, while still utilizing *MMC* as the only form of actuation.

2.2 Preliminary Theory

The objective of this section is to provide a basic understanding of the theory used as a basis for this work. Furthermore, mathematical operations used in this work are presented for those readers who might not necessarily be familiar with them. Furthermore, the novel work presented in **Chapter 3** is distinguished from the already established methodologies. This section also defines the notation used to represent various mathematical operations and variables.

2.2.1 Quaternions

Quaternions are commonly used in the spacecraft industry to describe the attitude of a body as they provide a redundant, nonsingular attitude description and are well suited to describe arbitrary, large rotations [14]. This provides notable advantages to the alternative option of Euler angles and rotation matrices.

In this work, quaternions are noted as $\hat{q} \in \mathbb{Q}$. Quaternions are composed of an ordered pair $\hat{q} = [q_0 \ \vec{q}]^T$, where q_0 is the quaternion scalar part and $\vec{q} = [q_1 \ q_2 \ q_3]^T$ is the quaternion vectorial part. Quaternions are named vector/pure quaternions and scalar quaternions if their scalar or vector part is zero, respectively. Furthermore, the special cases where quaternions are $[0 \ \vec{0}]^T$ or $[1 \ \vec{0}]^T$ will be denoted as $\hat{0}$ and $\hat{1}$, respectively.

Quaternions follow a particular set of operations and properties; these are discussed below as described in [15]:

Addition:

$$\hat{a} + \hat{b} = (a_0 + b_0, \vec{a} + \vec{b}) \in \mathbb{Q}$$

Scalar multiplication:

$$\hat{a}b = (a_0b, \vec{a}b) \in \mathbb{Q}$$

Multiplication:

$$\hat{a} \otimes \hat{b} = (a_0b_0 - \vec{a} \cdot \vec{b}, a_0\vec{b} + b_0\vec{a} + \vec{a} \times \vec{b}) \in \mathbb{Q}$$

Dot product:

$$\hat{a} \cdot \hat{b} = (a_0b_0 + \vec{a} \cdot \vec{b}, \vec{0}) \in \mathbb{Q}^s$$

Cross product:

$$\hat{a} \times \hat{b} = (0, a_0\vec{b} + b_0\vec{a} + \vec{a} \times \vec{b}) \in \mathbb{Q}^v$$

Conjugate:

$$\hat{a}^* = (a_0, -\vec{a}) \in \mathbb{Q}$$

Norm Square:

$$\|\hat{a}\|^2 = \hat{a} \otimes \hat{a}^* = (a_0^2 + \vec{a} \cdot \vec{a}, \vec{0}) \in \mathbb{Q}^s$$

If a quaternion norm is equal to $\hat{1}$, then the quaternion is referred to as a unit quaternion.

Attitude representation can be described using unit quaternions. Assuming two frames A and B , the relative attitude of frame B to the A frame can be represented using unit quaternions as follows.

$$\hat{q}_{A \rightarrow B} = \begin{bmatrix} \cos(\frac{\phi}{2}) \\ \sin(\frac{\phi}{2})\vec{n} \end{bmatrix} \quad (2.1)$$

Where $\vec{n} \in \mathbb{R}^3$ is a unit vector about which the A frame is rotated by an angle $\phi \in \mathbb{R}$ to obtain the B frame. Quaternions can also be used to propagate the attitude of frame B with respect to frame A with the rotational kinematic first-order differential equation shown

below:

$$\dot{\hat{q}}_{A \rightarrow B} = \frac{1}{2} \hat{q}_{A \rightarrow B} \otimes \hat{\omega}_{B/A}^B = \frac{1}{2} \hat{\omega}_{B/A}^A \otimes \hat{q}_{A \rightarrow B} \quad (2.2)$$

Here, $\hat{\omega}_{B/A}^B$ is a vector quaternion representing the angular velocity of the frame B to the A frame as seen in the B frame. This notation is to be used for the rest of this work. Furthermore, the time derivative of the quaternion can also be divided into its scalar and vectorial parts, as shown below:

$$\vec{q}_{A \rightarrow B} = \frac{1}{2} ((\vec{q}_{A \rightarrow B})^\times + q_{A \rightarrow B_0} I_{3 \times 3}) \vec{\omega}_{B/A}^B \quad (2.3)$$

$$q_{A \rightarrow B_0} = -\frac{1}{2} \vec{q}_{A \rightarrow B}^T \vec{\omega}_{B/A}^B \quad (2.4)$$

This vectorial notation can be beneficial to perform certain algebraic operations and is to be used in this work. If a third frame C is defined, whose attitude is known with respect to the A frame, that is, $\hat{q}_{A \rightarrow C}$ is known. Then, one can obtain the quaternion representing the relative position of the C frame with respect to the B frame, also known as quaternion error.

$$\hat{q}_{C \rightarrow B} = \hat{q}_{A \rightarrow C}^* \otimes \hat{q}_{A \rightarrow B} \quad \hat{q}_{B \rightarrow C} = \hat{q}_{A \rightarrow B}^* \otimes \hat{q}_{A \rightarrow C} \quad (2.5)$$

Here, the conjugate of an attitude quaternion represents the opposite rotation, this is:

$$\hat{q}_{C \rightarrow B}^* = \hat{q}_{B \rightarrow C} \quad (2.6)$$

Furthermore, any vector represented in the A frame can be rotated to the B frame using quaternion rotation operations. This is, creating a vector quaternion \hat{v}^A represented in the A frame, with the vector \vec{v}^A as its vector part, one can obtain the same vector quaternion represented in the B frame \hat{v}^B , and vice versa.

$$\hat{v}^B = \hat{q}_{A \rightarrow B}^* \otimes \hat{v}^A \otimes \hat{q}_{A \rightarrow B} \quad \hat{v}^A = \hat{q}_{A \rightarrow B} \otimes \hat{v}^B \otimes \hat{q}_{A \rightarrow B}^* \quad (2.7)$$

2.2.2 Model Reference Adaptive Control

This section presents the basis of Model Reference Adaptive Control (*MRAC*). This is the approach that is used to derive the adaptive control and estimation laws in this work. This section briefly introduces the main principle of *MRAC*, but will be further explained **Chapter 3**. *MRAC*'s principle is the creation of a reference or desired model that the system is forced to follow [13, 16]. The error between system and reference outputs is used as the feedback of the control and estimation laws.

The *MRAC* in this research is applied to a multi-input multi-output (*MIMO*) nonlinear system in the form described in [16].

$$\dot{\vec{x}} = A\vec{x} + B\vec{u}$$

where $\vec{x} \in \mathbb{R}^n$ is the state of the system available for feedback, $\vec{u} \in \mathbb{R}^m$ is the control input to be designed, and $B \in \mathbb{R}^{n \times m}$ and $A \in \mathbb{R}^{n \times n}$ are the known control matrix and unknown system matrix, with the pair (A, B) being controllable.

A reference or desired model is then created in the form:

$$\dot{\vec{x}}_d = A_d\vec{x}_d + B_d\vec{r}$$

where $\vec{r}(t) \in \mathbb{R}^m$ is a bounded command, and $A_d \in \mathbb{R}^{n \times n}$ is a Hurwitz reference state matrix that ensures \vec{x}_d is bounded. Then, using Lyapunov stability theory, a control law $\vec{u}(t)$ must be selected, which ensures the tracking error $\vec{e}(t) = \vec{x}(t) - \vec{x}_d(t)$ will asymptotically converge to zero.

2.2.3 Relevant Mathematical Operations

This section presents other mathematical operations and properties that are relevant to this work.

Skew-Symmetric Operator

Skew-symmetric matrices of a vector $\vec{v} \in \mathbb{R}^3$ shall be defined with the superscript (\times) , appearing as v^\times .

$$v^\times = \begin{bmatrix} 0 & -v_3 & v_2 \\ v_3 & 0 & -v_1 \\ -v_2 & v_1 & 0 \end{bmatrix}$$

The skew-symmetric matrices are singular by nature, meaning that these are non-invertible.

Diagonal Operator

In this work, a matrix with diagonal components defined by a vector $\vec{v} \in \mathbb{R}^n$ is represented by $\text{diag}(\vec{v}) \in \mathbb{R}^{n \times n}$ such that:

$$\text{diag}(\vec{v}) = \begin{bmatrix} v_1 & 0 & \dots & 0 \\ 0 & v_2 & \dots & 0 \\ \dots & \dots & \dots & 0 \\ 0 & 0 & 0 & v_n \end{bmatrix}$$

Projection Operator

As described by Roman in [17], the projection operator, denoted as P in this work, is a type of idempotent linear operator related to direct sums, thus it satisfies $P^2 = P$. The projection operator is used in this work to obtain the projection of any three-dimensional vector $\vec{v}^B \in \mathbb{R}^3$ represented in the B frame to the subspace defined by the direction of the gravitational field $\vec{v}_g^B \in \mathbb{R}$ as defined in the B frame, and the plane orthogonal to the gravitational field $\vec{v}_p^B \in \mathbb{R}^2$, in the B frame. This allows the separation of the controllable and uncontrollable subspaces of the system, which are defined in the I frame while working with the equations of motion as represented in the B frame.

Any vector \vec{v}^B represented in the B frame can be defined as the sum of its perpendicular

(\vec{v}_p) and parallel (\vec{v}_g) components with respect to the gravity vector, such that:

$$\vec{v}^B = \vec{v}_p^B + \vec{v}_g^B = P_p \vec{v}^B + P_g \vec{v}^B \quad (2.8)$$

where P_p is the projection operator to the two-dimensional subspace defined by the plane perpendicular to the gravity vector, and P_g is the projection operator to the one-dimensional subspace defined by the gravity vector. P_p and P_g are defined as in Eq. (2.9) and Eq. (2.10) respectively.

$$P_p = \left[I_{3 \times 3} - \frac{\vec{g}^B (\vec{g}^B)^T}{\|\vec{g}^B\|^2} \right] \quad (2.9)$$

$$P_g = \frac{\vec{g}^B (\vec{g}^B)^T}{\|\vec{g}^B\|^2} \quad (2.10)$$

Schur Complement

Let M be a block matrix defined as:

$$M = \begin{bmatrix} A & B \\ C & D \end{bmatrix}$$

where, A, B, C , and D are also matrices. Then, the Schur complement of A into M is defined as:

$$M|A = D - C^T A^{-1} B \quad (2.11)$$

If $A > 0$, then as stated by Zhang in [18], M will be positive definite if and only if its Schur complement is positive definite. That is:

$$M > 0 \iff M|A = D - C^T A^{-1} B > 0 \quad (2.12)$$

2.2.4 Lyapunov Stability

Stability proof of equilibrium points in dynamical systems is essential for control design. Equilibrium points of a system are characterized as unstable, stable, and asymptotically

stable. Unstable equilibrium points are those whose solutions that start in an arbitrary vicinity region do not stay in that same region. Stable equilibrium points, on the contrary, are those whose solutions starting on the arbitrary vicinity region will remain there. Finally, asymptotically stable equilibrium points are characterized by their solutions approaching the equilibrium point as time approaches infinity. The stability of equilibrium points is almost always characterized using the Lyapunov Stability Theory.

Linear time-invariant systems' $\dot{\vec{x}} = A\vec{x}$ equilibrium points can easily be categorizable by direct analysis of the eigenvalues of the A matrix. However, non-linear systems present more challenges when it comes to the stability analysis of their equilibrium points. Lyapunov Stability Theorems are used for these systems. This section briefly introduces these theorems as described by Khalil in [19].

Theorem 2.2.4.1

For a system described by $\dot{x} = f(x)$, let $x = 0$ be an equilibrium point and $D \subset \mathbb{R}^n$ be a domain containing $x = 0$. Let $V : D \rightarrow \mathbb{R}$ be a radially unbounded and continuously differentiable function such that

$$V(0) = 0 \quad \& \quad V(x) > 0 \in D - \{0\}$$

$$\dot{V}(x) \leq 0 \in D$$

Then, $x = 0$ is stable. Moreover, if

$$\dot{V}(x) < 0 \in D - \{0\}$$

then $x = 0$ is asymptotically stable.

2.2.5 Barbalat's Lemma

Barbalat's Lemma can be used if the Lyapunov stability analysis leads to a stability conclusion but fails to prove asymptotic stability. That is, for a $V(\vec{x}) > 0$ and $\dot{V}(\vec{x}) \leq 0$,

there is an extended analysis that can prove convergence of the state parameters \vec{x} . In this research, Barbalat's Lemma is used as an extension to the Lyapunov stability analysis to conclude the asymptotic stability of the parameters. The definition for Barbalat's Lemma is shown below as described by Lavretsky and Wise in [13].

Theorem 2.2.5.1

Let $f : R \rightarrow R$ be a uniformly continuous function on $[0, \infty)$. Suppose that,

$$\lim_{t \rightarrow \infty} \int_0^t f(\tau) d\tau$$

exists and is finite. Then, $\lim_{t \rightarrow \infty} f(t) = 0$.

If Barbalat's Lemma is applied to a continuously differentiable function such as a Lyapunov function $V(\vec{x})$, [13] states the following.

Theorem 2.2.5.2

Let $f : R \rightarrow R$ be continuously differentiable on $[0, \infty)$, and suppose that $\lim_{t \rightarrow \infty} f(t)$ exists and is finite. If the function derivative $\dot{f}(t)$ is uniformly continuous on $[0, \infty)$, then $\lim_{t \rightarrow \infty} \dot{f}(t) = 0$.

From this second theorem, [13] derives the corollary that is used for the stability extension of the Lyapunov conclusion using Barbalat's Lemma.

Theorem 2.2.5.3

If a scalar function $f : R \rightarrow R$ is twice continuously differentiable on $[0, \infty)$ and has a finite limit,

$$\lim_{t \rightarrow \infty} f(t) < \infty$$

and the second derivative is bounded, then

$$\lim_{t \rightarrow \infty} \dot{f}(t) = 0$$

If $f(t)$ is defined as the Lyapunov function $V(\vec{x})$, then one can apply **Theorem 2.2.5.3** to conclude that the $\lim_{t \rightarrow \infty} \dot{V}(\vec{x}) = 0$ as long as $\ddot{V}(\vec{x})$ is bounded.

3 Methodology

This chapter presents the approach used to solve the estimation and control problem. The procedure is divided into two main sections. **Section 3.1** dives into the derivation of the equations of motion (*EOM*) describing the kinematic and kinetic behavior of the system in terms of first-order differential equations. The section also provides information on the reference trajectory (i.e., desired dynamics) design, essential in *MRAC*. Finally, the error dynamics between the derived *B* frame dynamics and designed *D* frame trajectory, which is the error to be minimized in order for the system to follow the desired signals. **Section 3.2** presents the adaptive control and estimation update laws, followed by the stability proof in the sense of Lyapunov, with an extension using Barbalat's Lemma to demonstrate asymptotic stability.

3.1 Dynamics Formulation

This section introduces the dynamics that describe the behavior of the body, as well as the reference or desired trajectory required to obtain the adaptive control and estimation laws. Finally, the equations of motions that represent the behavior of the *B* frame with respect to the *D* frame are defined.

3.1.1 Testbed Dynamics

The 5-DOF spacecraft simulator rotational motion can be modeled using Euler's equations of motion, assuming a rigid body as shown in Eq. (3.1). Here, angular momentum (\vec{H}) is defined as in Eq. (3.2).

$$\vec{\tau}_{ext}^B = \dot{\vec{H}}_{B/I}^B + \vec{\omega}_{B/I}^B \times \vec{H}_{B/I}^B \quad (3.1)$$

$$\vec{H}_{B/I}^B = J^B(t) \vec{\omega}_{B/I}^B \quad (3.2)$$

Here, $\vec{\tau}_{ext}^B$ represents the external torque acting on the body, and $\vec{\omega}_{B/I}^B$ are the angular rates of the testbed with respect to the inertial frame represented in the body fixed frame. In Eq. (3.2), the moment of inertia matrix $J^B(t)$ is time-varying and positive definite, thus

invertible for all time t . The variation in $J^B(t)$ is due to the movement of the shifting masses, which not only has an effect on the position of the *CoM* but also affects the *MoI*.

Furthermore, the attitude of the body can be defined through quaternion representation, previously introduced in **Section 2.2**. Recall then from Eq. (2.2), the kinematic equation that represents the attitude of the body fixed frame with respect to the inertial frame using quaternions

$$\dot{\hat{q}}_{I \rightarrow B} = \frac{1}{2} \hat{q}_{I \rightarrow B} \otimes \hat{\omega}_{B/I}^B \quad (3.3)$$

where $\hat{q}_{I \rightarrow B}$ is the attitude quaternion which represents the frame rotation from the inertial frame to the body-fixed frame, and $\hat{\omega}_{B/I}^B$ is a vector quaternion with $\vec{\omega}_{B/I}^B$ as its vector part.

3.1.2 Moment of Inertia of the Testbed

One can define the testbed's time-varying moment of inertia as:

$$J^B(t) = J_0^B + J_m^B(\sigma(t)) \quad (3.4)$$

$$J_0^B = J_0^{CoM} - M(\vec{r}_{off0})^\times (\vec{r}_{off0})^\times - \sum_{i=1}^3 m_i (\vec{r}_{i0})^\times (\vec{r}_{i0})^\times \quad (3.5)$$

$$J_m^B(\sigma(t)) = - \sum_{i=1}^3 m_i (\sigma_i(t))^\times (\sigma_i(t))^\times \quad (3.6)$$

Here, J_0^B represents the initial *MoI* of the 5-DOF before the control maneuver is initiated. This time-invariant moment of inertia is derived as in Eq. (3.5) and can be visualized in Figure 3.1, and includes the *MoI* of the main body about its *CoM*₀. Then, using the parallel-axis theorem, one can translate the moment of inertia from points *CoM*₀ to *CoM*_d to obtain the *MoI* about the desired point, in this case, the *CoM*_d is the *CoR* of the testbed. Furthermore, the sliding masses are treated as point masses. In that case, one can determine their moment of inertia about the *CoM*_d using the summation of each mass inertia as shown in the last term of Eq. (3.5). In this case, the masses' initial position to the *CoM*_d is used, which is time-invariant. On the other hand, $J_m^B(\sigma(t))$ is the time-varying *MoI* due to the

change in the sliding mass position (σ_i) of the i^{th} sliding mass (m_i) as displayed in Figure 3.1 and derived in Eq. (3.5). In this case, the MoI is taken for each mass with respect to its initial position, thus simplifying the time-varying aspect of $J^B(t)$. The following assumptions are made when deriving the dynamics of the 5-DOF testbed.

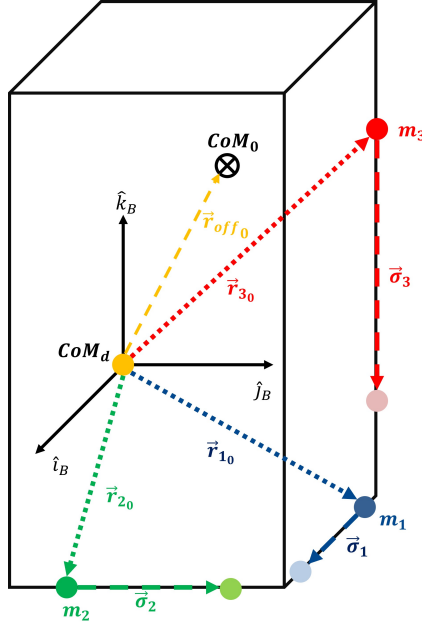


Figure 3.1 MoI schematic for the derivation of the different contributing components.

Assumption 1. The body-fixed frame is aligned with the principal axes of the 5-DOF.

Assumption 2. Sliding masses move along the principal axes of the 5-DOF, thus $J_m(\sigma(t))$ has no off-diagonal terms.

Recalling **Assumption 1**, $\vec{\sigma}$ is defined as in Eq. (3.7). Substituting $\vec{\sigma}$ into Eq. (3.6) the matrix form of MoI generated by the sliding masses J_m is defined as in Eq. (3.8).

$$\vec{\sigma} \equiv \begin{bmatrix} r_{x_1} \\ r_{y_2} \\ r_{z_3} \end{bmatrix}, \quad \vec{r}_x = \begin{bmatrix} \sigma_1 \\ 0 \\ 0 \end{bmatrix}, \quad \vec{r}_y = \begin{bmatrix} 0 \\ \sigma_2 \\ 0 \end{bmatrix}, \quad \vec{r}_z = \begin{bmatrix} 0 \\ 0 \\ \sigma_3 \end{bmatrix} \quad (3.7)$$

$$J_m^B(\sigma(t)) = \begin{bmatrix} \sigma_2^2 + \sigma_3^2 & 0 & 0 \\ 0 & \sigma_1^2 + \sigma_3^2 & 0 \\ 0 & 0 & \sigma_1^2 + \sigma_2^2 \end{bmatrix} \quad (3.8)$$

Recalling Eq. (3.4) and substituting the expression on Eq. (3.8), one can obtain the time-varying *MoI* expression in matrix form as in Eq. (3.9).

$$J^B(t) = \begin{bmatrix} J_{0xx} + \sigma_2^2 + \sigma_3^2 & 0 & 0 \\ 0 & J_{0yy} + \sigma_1^2 + \sigma_3^2 & 0 \\ 0 & 0 & J_{0zz} + \sigma_1^2 + \sigma_2^2 \end{bmatrix} \quad (3.9)$$

Taking the first time derivative of Eq. (3.8), the following equation is obtained.

$$\dot{J}_m^B(\sigma(t)) = 2 \begin{bmatrix} \sigma_2\dot{\sigma}_2 + \sigma_3\dot{\sigma}_3 & 0 & 0 \\ 0 & \sigma_1\dot{\sigma}_1 + \sigma_3\dot{\sigma}_3 & 0 \\ 0 & 0 & \sigma_1\dot{\sigma}_1 + \sigma_2\dot{\sigma}_2 \end{bmatrix} \quad (3.10)$$

Eq. (3.10) will be required for the control law design presented later in this chapter.

3.1.3 External Torques acting on the Testbed

In the real system, multiple external torques affect the 5-DOF testbed. However, for this work, friction and aerodynamic torques acting on the testbed have been neglected due to the minimal effect of these with respect to the main disturbance acting on the body in gravity-induced torque. The main external torque ($\vec{\tau}_{ext}$) acting on the body is the result of the gravity force and offset between the *CoM* and *CoR* of the testbed, which is defined in Eq. (3.11) and can be visualized in Figure 3.2

$$\vec{\tau}_{ext}^B = \vec{r}_{off}^B \times M\vec{g}^B \quad (3.11)$$

where \vec{r}_{off}^B represents the offset between *CoM* and *CoR* at any time (t), M is the total mass of the testbed, and \vec{g}^B is the gravitational acceleration represented in the body fixed frame,

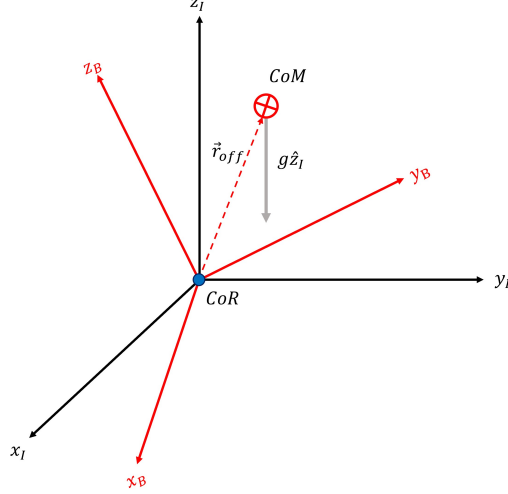


Figure 3.2 Schematic of I and B frames, with gravity vector acting on the offset CoM .

which is time-varying as it is a function of the attitude error between the body-fixed frame and the inertial frame. The transformation can be obtained using quaternion frame rotation, as shown below.

$$\hat{g}^B = \hat{q}_{I \rightarrow B}^* \otimes \hat{g}^I \otimes \hat{q}_{I \rightarrow B} \quad (3.12)$$

Here, $(^*)$ indicates the quaternion conjugate, the definition of which can be found in **Section 2.2.1**. Furthermore, both $\hat{g}^B = [0 \ (\vec{g}^B)^T]^T$ and $\hat{g}^I = [0 \ (\vec{g}^I)^T]^T = [\vec{0}_{3 \times 1} \ -g]^T$ are vector quaternions represented in the body-fixed and inertial frames respectively. Recalling the definition from **Section 2.2.1** in **Chapter 2**, these are then quaternions with zero scalar part.

If this is to be treated as a control problem, one must have control authority over the system's dynamics. It has already been stated that the torque generated by the system is due to the interaction between \vec{r}_{off} and \vec{g} . Therefore, the testbed's dynamics can be controlled by modifying the position of \vec{r}_{off} . If the initial $\vec{r}_{off}(t_0)$ is defined as $\vec{\Theta}$, representing the CoM to CoR offset prior to the control and estimation maneuvers. This provides two benefits. Firstly, defining a constant unknown simplifies the stability analysis. Secondly, separating the gravity torque into two separate terms allows to define the position of the sliding masses as the control input. The control input as a function of the sliding mass positions can be

added as in Eq. (3.13) if the following assumption is made:

Assumption 3. All sliding masses are equal in mass (m).

$$\vec{\tau}_{ext} = \vec{\Theta} \times M \vec{g}^B + \vec{\sigma}(t) \times m \vec{g}^B \quad (3.13)$$

where $\vec{\Theta}$ represents the initial *CoM* to *CoR* offset, M is the total mass of the spacecraft simulator, including all three sliding masses, and m represents the mass of the sliding masses following **Assumption 3**. For simplification, $\vec{u}(\sigma)$ represents the control input on the system as a function of the position of the sliding masses, as shown in Eq. (3.14).

$$\vec{u}(\sigma) = m (-\vec{g}^B(t) \times \vec{\sigma}) \quad (3.14)$$

Furthermore, borrowing the notation from [9], one can define Φ as in Eq. (3.15) so that it satisfies the linear parametrization property, $\Phi \vec{\Theta} = \vec{\Theta} \times M \vec{g}^B$.

$$\Phi = -M (\vec{g}^B)^\times \quad (3.15)$$

Recalling Eq. (3.1), and substituting in Eq. (3.2), Eq. (3.4), and Eq. (3.13), the first order differential equation describing the rate of change of the body angular rates is obtained as

$$\begin{aligned} \Phi \vec{\Theta} + \vec{u}(\sigma) &= \frac{d}{dt} (J^B(t) \vec{\omega}_{B/I}^B) + \vec{\omega}_{B/I}^B \times J^B(t) \vec{\omega}_{B/I}^B \\ \Phi \vec{\Theta} + \vec{u}(\sigma) &= J^B(t) \vec{\omega}_{B/I}^B + J^B(t) \dot{\vec{\omega}}_{B/I}^B + \vec{\omega}_{B/I}^B \times J^B(t) \vec{\omega}_{B/I}^B \\ \dot{\vec{\omega}}_{B/I}^B &= (J^B(t))^{-1} \left[-J_m^B(t) \vec{\omega}_{B/I}^B - \vec{\omega}_{B/I}^B \times J^B(t) \vec{\omega}_{B/I}^B + \Phi \vec{\Theta} + \vec{u}(\sigma) \right] \end{aligned} \quad (3.16)$$

3.1.4 Desired Dynamics

To design an adaptive-based control law that allows estimation of $\vec{\Theta}$, one must create a reference trajectory for the system to follow. It has been shown that the system has no control authority over the \hat{z}^I axis in the inertial frame. Therefore the desired dynamics have been designed to ensure that the angular velocity follows $\dot{\vec{\omega}}_{D/I_z}^I = 0 \forall t$, and $\vec{\omega}_{D/I_z}^I = \vec{\omega}_{B/I_z}^I$.

This is the angular rates of the B and D frames remain equal for all time. Then, the desired angular rates are defined to obtain observability of the unknowns as follows. We shall design the first control maneuver to follow Eq. (3.17).

$$\vec{\omega}_{D/I}^D = R_{I \rightarrow D} \begin{bmatrix} 0 \\ 0 \\ \omega_{B/I_z}^I \end{bmatrix} \quad \forall t \notin \{T_1, T_2\} \quad (3.17)$$

$$\dot{\hat{q}}_{I \rightarrow D} = \frac{1}{2} \hat{q}_{I \rightarrow D} \otimes \vec{\omega}_{D/I}^D \quad (3.18)$$

However, two different stable attitudes are required to converge the unknown parameters to their true values. The first attitude objective is defined by the initial conditions IC of the B frame. This is defining the IC of the D frame as follows:

$$\vec{q}_{I \rightarrow D}(t_0) = P_g \vec{q}_{I \rightarrow B}(t_0) \quad (3.19)$$

This will lead to the xy-planes of the D and I frames to be aligned. However, adding a rotation about the z-axis of the D frame with respect to the I frame that ensures the x and y axes of the B frame projected to the inertial xy-plane are aligned with the x and y axes of the D frame. This will lead to a desired trajectory that maintains the z-axis of the D and I frames aligned during the first attitude maneuver while ensuring the $\lim_{t \rightarrow \infty} \hat{q}_{D \rightarrow B} = \hat{1}$. The second attitude objective will drive the desired trajectory to a pure spin about the I frame z-axis, with a predefined and constant angular error ψ between the xy-planes of the D and I frames. Therefore for attitude to be achieved, the desired trajectory will be defined as in Eq. (3.20) in the interval defined by $T_1 \leq t \leq T_2$.

$$\vec{\omega}_{D/I}^D = R_{I \rightarrow D} \begin{bmatrix} 0 \\ 0 \\ \omega_{B/I_z}^I \end{bmatrix} + \begin{bmatrix} 0 \\ \omega_{D/I_e}^D \\ 0 \end{bmatrix} \quad \forall t \in \{T_1, T_2\} \quad (3.20)$$

Here, ω_{D/I_e}^D is the angular velocity defined in the y-axis of the D frame to obtain an angular error ψ which is defined by solving the integral in Eq. (3.21).

$$\psi = \int_{T_1}^{T_2} \omega_{D/I_e}^D = \int_{T_1}^{T_2} A \sin\left(\frac{\pi}{T_2 - T_1}(t - T_1)\right) dt \quad (3.21)$$

Which ensures that $\vec{\omega}_{D/I_e}^D(T_1) = \vec{\omega}_{D/I_e}^D(T_2) = 0$. Then solving for the amplitude A , one can obtain the angular displacement ψ in the interval $T_2 - T_1$, shown in Eq. (3.22).

$$A = \frac{\psi\pi}{2(T_2 - T_1)} \quad (3.22)$$

Then, for $t > T_2$, the desired trajectory will remain spinning solely about the I frame z-axis.

3.1.5 Error Dynamics

After obtaining the reference model dynamics, the error between trajectories is presented in this subsection, followed by the error dynamics derivation. The relative angular rates of the testbed with respect to the desired frame $\vec{\omega}_{B/D}^B$ are defined as in Eq. (3.23).

$$\vec{\omega}_{B/D}^B = \vec{\omega}_{B/I}^B - \vec{\omega}_{D/I}^B \quad (3.23)$$

As it can be observed from the derivation in **Section 3.1.4**, Eq. (3.17) and Eq. (3.20) are obtained in the desired frame, thus it is required to perform the frame rotation from the desired frame to the body-fixed frame to obtain the relative velocity between the B and D represented in the B frame. For it, one must define the quaternion error between the desired and body-fixed frames using the quaternion error equation introduced in **Section 2.2.1**.

$$\hat{q}_{D \rightarrow B} = \hat{q}_{I \rightarrow D}^* \otimes \hat{q}_{I \rightarrow B} \quad (3.24)$$

Also, recall that $\hat{q}_{B \rightarrow D} = \hat{q}_{D \rightarrow B}^* = \hat{q}_{I \rightarrow B}^* \otimes \hat{q}_{I \rightarrow D}$. One can then rewrite Eq. (3.23) as shown below in terms of vectorial quaternions:

$$\hat{\omega}_{B/D}^B = \hat{\omega}_{B/I}^B - \hat{q}_{D \rightarrow B}^* \otimes \hat{\omega}_{D/I}^D \otimes \hat{q}_{D \rightarrow B} = \hat{\omega}_{B/I}^B - \hat{q}_{B \rightarrow D} \otimes \hat{\omega}_{D/I}^D \otimes \hat{q}_{B \rightarrow D}^* \quad (3.25)$$

Taking the derivative with respect to time of both sides of Eq. (3.25), we obtain the following expression:

$$\begin{aligned} \dot{\hat{\omega}}_{B/D}^B &= \dot{\hat{\omega}}_{B/I}^B - \hat{q}_{B \rightarrow D} \otimes \dot{\hat{\omega}}_{D/I}^D \otimes \hat{q}_{B \rightarrow D}^* - \dot{\hat{q}}_{B \rightarrow D} \otimes \hat{\omega}_{D/I}^D \otimes \hat{q}_{B \rightarrow D}^* - \hat{q}_{B \rightarrow D} \otimes \dot{\hat{\omega}}_{D/I}^D \otimes \dot{\hat{q}}_{B \rightarrow D}^* \\ \dot{\hat{\omega}}_{B/D}^B &= \dot{\hat{\omega}}_{B/I}^B - \hat{q}_{B \rightarrow D} \otimes \dot{\hat{\omega}}_{D/I}^D \otimes \hat{q}_{B \rightarrow D}^* + \frac{1}{2} \hat{\omega}_{B/D}^B \otimes \hat{q}_{B \rightarrow D} \otimes \hat{\omega}_{D/I}^D \otimes \hat{q}_{B \rightarrow D}^* - \frac{1}{2} \hat{q}_{B \rightarrow D} \otimes \hat{\omega}_{D/I}^D \otimes \hat{q}_{B \rightarrow D}^* \otimes \hat{\omega}_{B/D}^B \\ \dot{\hat{\omega}}_{B/D}^B &= \dot{\hat{\omega}}_{B/I}^B - \hat{q}_{B \rightarrow D} \otimes \dot{\hat{\omega}}_{D/I}^D \otimes \hat{q}_{B \rightarrow D}^* + \frac{1}{2} (\hat{\omega}_{B/D}^B \otimes \hat{\omega}_{D/I}^B - \hat{\omega}_{D/I}^B \otimes \hat{\omega}_{B/D}^B) \\ \dot{\hat{\omega}}_{B/D}^B &= \dot{\hat{\omega}}_{B/I}^B - \hat{q}_{D \rightarrow B}^* \otimes \dot{\hat{\omega}}_{D/I}^D \otimes \hat{q}_{D \rightarrow B} - \hat{\omega}_{D/I}^D \otimes \hat{\omega}_{B/D}^B \end{aligned} \quad (3.26)$$

Note that since $\hat{\omega}_{D/I}^B$ and $\hat{\omega}_{B/D}^B$ are both vector quaternions, the following property can be applied: $\hat{a} \otimes \hat{b} = -\hat{b} \otimes \hat{a}$. Then, Eq. (3.26) can be rewritten in vectorial form:

$$\dot{\hat{\omega}}_{B/D}^B = \dot{\hat{\omega}}_{B/I}^B - \dot{\hat{\omega}}_{D/I}^B - \vec{\omega}_{D/I}^B \times \vec{\omega}_{B/D}^B \quad (3.27)$$

Plugging Eq. (3.16) into Eq. (3.27) and multiplying both sides by J^B , the first order differential equation describing the rate of change of the angular rates of the B frame with respect to the D frame is obtained in Eq. (3.28).

$$J^B \dot{\hat{\omega}}_{B/D}^B = -J_m^B \vec{\omega}_{B/I}^B - \vec{\omega}_{B/I}^B \times J^B \vec{\omega}_{B/I}^B + \Phi \vec{\Theta} + \vec{u}_\sigma - J^B \dot{\hat{\omega}}_{D/I}^B - J^B (\vec{\omega}_{D/I}^B \times \vec{\omega}_{B/D}^B) \quad (3.28)$$

3.2 Adaptive Estimation & Control Design

This section presents the adaptive control and estimation laws as well as the stability proof of the system. The adaptive control and update laws obtained through Lyapunov

stability analysis are presented in Eq. (3.29) and Eq. (3.30) respectively.

$$\begin{aligned} \vec{u} \equiv & P_p \left[-J_m^B \left(\frac{1}{2} \vec{r} - \vec{\omega}_{B/I}^B \right) + (\vec{\omega}_{B/I}^B \times J^B \vec{\omega}_{B/I}^B) - \Phi \hat{\Theta} - K \vec{r} - \Psi \vec{r} \right] \\ & + P_p J^B \left(\dot{\vec{\omega}}_{D/I}^B + \vec{\omega}_{D/I}^B \times \vec{\omega}_{B/D}^B - \frac{1}{2} \alpha ((\vec{q}_{D \rightarrow B})^\times + q_{D \rightarrow B_0} I_{3 \times 3}) \vec{\omega}_{B/D}^B \right) \end{aligned} \quad (3.29)$$

$$\dot{\hat{\Theta}} \equiv \gamma \Phi^T \vec{r} \quad (3.30)$$

Here, $K > 0 \in \mathbb{R}^{3 \times 3}$ and $\gamma > 0 \in \mathbb{R}^{3 \times 3}$ are positive definite diagonal matrices, representing control gains and adaptive law learning rate respectively, and $\alpha > 0 \in \mathbb{R}$ is a scalar control tuning parameter. Furthermore, \vec{r} is the error sum of angular rates and attitude quaternion presented in **Section 3.2.1**, and $P_p \in \mathbb{R}^{3 \times 3}$ is the projection operator to the plane perpendicular to the gravitational field as defined in Eq. (2.9), and $\Psi \in \mathbb{R}^{3 \times 3}$ is a positive definite diagonal matrix defined by $\Psi = \text{diag}((P_p \hat{\Theta}) \odot (P_p \hat{\Theta}))$ and expanded in Eq. (3.31).

$$\Psi = \begin{bmatrix} \hat{\Theta}_{p_1}^2 & 0 & 0 \\ 0 & \hat{\Theta}_{p_2}^2 & 0 \\ 0 & 0 & \hat{\Theta}_{p_3}^2 \end{bmatrix} \quad (3.31)$$

3.2.1 Lyapunov Stability

Before starting the stability proof, and following the approach used by Woodward and Bevilacqua in [20], a new parameter \vec{r} is introduced in Eq. (3.32), which is the error sum of angular rates and attitude quaternion used to facilitate the Lyapunov stability analysis.

$$\vec{r} = \vec{\omega}_{B/D}^B + \alpha \vec{q}_{D \rightarrow B} \quad (3.32)$$

With the first time derivative $\dot{\vec{r}} = \dot{\vec{\omega}}_{B/D}^B + \alpha \dot{\vec{q}}_{D \rightarrow B}$. Substituting in Eq. (3.28) and following the definition of $\dot{\vec{q}}_{D \rightarrow B}$ from **Section 2.2.1**, $\dot{\vec{r}}$ takes the form presented in Eq. (3.33).

$$\dot{\vec{r}} = \dot{\vec{\omega}}_{B/I}^B - \dot{\vec{\omega}}_{D/I}^B - \vec{\omega}_{D/I}^B \times \vec{\omega}_{B/D}^B + \frac{1}{2} \alpha ((\vec{q}_{D \rightarrow B})^\times + q_{D \rightarrow B_0} I_{3 \times 3}) \vec{\omega}_{B/D}^B \quad (3.33)$$

The states required for the stability proof of the system are defined as:

$$\vec{x} = \begin{bmatrix} \vec{\omega}_{B/D}^B \\ \hat{q}_{D \rightarrow B} \\ \tilde{\Theta} \end{bmatrix} \quad (3.34)$$

The selection of positive definite Lyapunov function is the following:

$$V(\vec{x}) \equiv \frac{1}{2} \vec{r}^T J^B \vec{r} + \frac{1}{2} \tilde{\Theta}^T \gamma^{-1} \tilde{\Theta} + \beta [\vec{q}_{D \rightarrow B}^T \vec{q}_{D \rightarrow B} + (q_{D \rightarrow B_0} - 1)^2] > 0 \quad (3.35)$$

Where $\beta > 0 \in \mathbb{R}$. Recall that $J^B(t)$, although time-varying, it is by definition $J^B(t) > 0 \forall t$. As shown in **Section 2.2.4**, in order to prove stability of the system, the first time derivative of $V(\vec{x})$ is required to be at least negative semidefinite. $\dot{V}(\vec{x})$ from Eq. (3.35) is shown in Eq. (3.36).

$$\dot{V}(\vec{x}) = \frac{1}{2} \vec{r}^T J^B \vec{r} + \vec{r}^T J^B \dot{\vec{r}} + \tilde{\Theta}^T \gamma^{-1} \dot{\tilde{\Theta}} + 2\beta [\vec{q}_{D \rightarrow B}^T \dot{\vec{q}}_{D \rightarrow B} + (q_{D \rightarrow B_0} - 1) \dot{q}_{D \rightarrow B_0}] \quad (3.36)$$

Where $J^B = J_m^B$, and recalling that $\tilde{\Theta}(t) = \vec{\Theta} - \hat{\Theta}(t)$, the time derivative of the estimation error is $\dot{\tilde{\Theta}}(t) = -\dot{\hat{\Theta}}(t)$. Substituting in the expressions for $\dot{\vec{q}}_{D \rightarrow B}$ and $\dot{q}_{D \rightarrow B_0}$ as defined in **Section 2.2.1**, Eq. (3.36) becomes:

$$\dot{V}(\vec{x}) = \frac{1}{2} \vec{r}^T J_m^B \vec{r} + \vec{r}^T J^B \dot{\vec{r}} - \tilde{\Theta}^T \gamma^{-1} \dot{\tilde{\Theta}} + \beta \vec{q}_{D \rightarrow B}^T \vec{\omega}_{B/D}^B \quad (3.37)$$

The above Eq. (3.37) can be further expanded by substituting in the expression for $\dot{\vec{r}}$. Then, plugging in Eq. (3.27), substituting the expression for $\dot{\vec{q}}_{D \rightarrow B}$, and performing some linear

algebra, Eq. (3.38) is obtained.

$$\begin{aligned}
\dot{V}(\vec{x}) &= \frac{1}{2} \vec{r}^T \vec{j}_m^B \vec{r} + \vec{r}^T J^B \left[\dot{\vec{\omega}}_{B/D}^B + \alpha \dot{\vec{q}}_{D \rightarrow B} \right] - \tilde{\Theta}^T \gamma^{-1} \dot{\hat{\Theta}} + \beta \vec{q}_{D \rightarrow B}^T \vec{\omega}_{B/D}^B \\
&= \frac{1}{2} \vec{r}^T \vec{j}_m^B \vec{r} + \vec{r}^T \left[-\vec{j}_m^B \vec{\omega}_{B/I}^B - \vec{\omega}_{B/I}^B \times J^B \vec{\omega}_{B/I}^B + \Phi \vec{\Theta} + \vec{u} \right] \\
&\quad - \vec{r}^T J^B \left[\dot{\vec{\omega}}_{D/I}^B + \vec{\omega}_{D/I}^B \times \vec{\omega}_{B/D}^B - \frac{1}{2} \alpha ((\vec{q}_{D \rightarrow B})^\times + q_{D \rightarrow B_0} I_{3 \times 3}) \vec{\omega}_{B/D}^B \right] \\
&\quad - \gamma^{-1} \tilde{\Theta}^T \dot{\hat{\Theta}} + \beta \vec{q}_{D \rightarrow B}^T \vec{\omega}_{B/D}^B \\
&= \frac{1}{2} \vec{r}^T \vec{j}_m^B \vec{r} + \vec{r}^T \left[-\vec{j}_m^B \vec{\omega}_{B/I}^B - \vec{\omega}_{B/I}^B \times J^B \vec{\omega}_{B/I}^B + \Phi \hat{\Theta} + \vec{u} \right] \\
&\quad - \vec{r}^T J^B \left[\dot{\vec{\omega}}_{D/I}^B + \vec{\omega}_{D/I}^B \times \vec{\omega}_{B/D}^B - \frac{1}{2} \alpha ((\vec{q}_{D \rightarrow B})^\times + q_{D \rightarrow B_0} I_{3 \times 3}) \vec{\omega}_{B/D}^B \right] \\
&\quad + \tilde{\Theta}^T (\Phi^T \vec{r} - \gamma^{-1} \dot{\hat{\Theta}}) + \beta \vec{q}_{D \rightarrow B}^T \vec{\omega}_{B/D}^B
\end{aligned} \tag{3.38}$$

Plugging in the control and update law defined in Eq. (3.29) and Eq. (3.30) respectively leads to the following from of $\dot{V}(\vec{x})$.

$$\begin{aligned}
\dot{V}(\vec{x}) &= \vec{r}^T P_g \left[\vec{j}_m^B \left(\frac{1}{2} \vec{r} - \vec{\omega}_{B/I}^B \right) - (\vec{\omega}_{B/I}^B \times J^B \vec{\omega}_{B/I}^B) + \Phi \hat{\Theta} \right] \\
&\quad - \vec{r}^T P_g J^B \left[\dot{\vec{\omega}}_{D/I}^B + \vec{\omega}_{D/I}^B \times \vec{\omega}_{B/D}^B - \frac{1}{2} \alpha ((\vec{q}_{D \rightarrow B})^\times + q_{D \rightarrow B_0} I_{3 \times 3}) \vec{\omega}_{B/D}^B \right] \\
&\quad + \beta \vec{q}_{D \rightarrow B}^T \vec{\omega}_{B/D}^B - \vec{r}^T P_p K \vec{r} - \vec{r}^T P_p \Psi \vec{r}
\end{aligned} \tag{3.39}$$

where P_g is the projection operator $\mathbb{R}^3 \rightarrow \mathbb{R}$ to the gravity vector defined in Eq. (2.10). Recalling from **Section 2.2.3** that all projection matrices are by definition symmetric, therefore $P_g = P_g^T$. Furthermore, moment of inertia tensors are, by definition symmetric. Therefore, $\dot{V}(\vec{x})$ can be rewritten as:

$$\begin{aligned}
\dot{V}(\vec{x}) &= \left[\vec{j}_m^B \left(\frac{1}{2} \vec{r} - \vec{\omega}_{B/I}^B \right) - (\vec{\omega}_{B/I}^B \times J^B \vec{\omega}_{B/I}^B) + \Phi \hat{\Theta} \right]^T P_g \vec{r} \\
&\quad - \left[\dot{\vec{\omega}}_{D/I}^B + \vec{\omega}_{D/I}^B \times \vec{\omega}_{B/D}^B - \frac{1}{2} \alpha ((\vec{q}_{D \rightarrow B})^\times + q_{D \rightarrow B_0} I_{3 \times 3}) \vec{\omega}_{B/D}^B \right]^T J^B P_g \vec{r} \\
&\quad + \beta \vec{q}_{D \rightarrow B}^T \vec{\omega}_{B/D}^B - \vec{r}^T P_p K \vec{r} - \vec{r}^T P_p \Psi \vec{r}
\end{aligned}$$

Then, $P_g \vec{r} = P_g(\vec{\omega}_{B/D}^B + \alpha \vec{q}_{D \rightarrow B}) = \vec{0}$ can be proven as follows. Recalling from **Section 3.1.4**, the definition for the desired trajectory in Eq. (3.17), where the D frame has been designed such that the z-axis component of the angular rates of the BF and D frames are $\vec{\omega}_{D/I_z}^I = \vec{\omega}_{B/I_z}^I \forall t$. Therefore $P_p \vec{\omega}_{B/D}^B = 0 \forall t$. Furthermore, in **Section 2.2.1**, it has been shown that $\vec{q}_{D \rightarrow B} = \sin(\phi/2) \vec{n}$. Where, \vec{n} represents the vector about which the body is rotating by an angle ϕ to go from the D to B frame. Therefore, due to the definition of the D frame, spinning purely about the I frame z-axis, $P_g \vec{r} = \vec{0}$. Which leads to Eq. (3.40):

$$\begin{aligned}
\dot{V}(\vec{x}) &= \beta \vec{q}_{D \rightarrow B}^T \vec{\omega}_{B/D}^B - \vec{r}^T P_p K \vec{r} - \vec{r}^T P_p \Psi \vec{r} \\
&= \beta (\vec{q}_{D \rightarrow B_p} + \vec{q}_{D \rightarrow B_g})^T (\vec{\omega}_{B/D_p}^B + \vec{\omega}_{B/D_g}^B) \\
&\quad - \vec{r}^T P_p K \vec{r} - \vec{r}^T P_p \Psi \vec{r} \\
&= \beta \vec{q}_{D \rightarrow B_p}^T \vec{\omega}_{B/D_p}^B - \vec{r}^T P_p K \vec{r} - \vec{r}^T P_p \Psi \vec{r} \\
&= -\vec{r}^T P_p \Psi \vec{r} - (\vec{\omega}_{B/D}^B + \alpha \vec{q}_{D \rightarrow B})^T P_p K (\vec{\omega}_{B/D}^B + \alpha \vec{q}_{D \rightarrow B}) \\
&\quad + \beta \vec{q}_{D \rightarrow B_p}^T \vec{\omega}_{B/D_p}^B \\
&= -\vec{r}^T P_p \Psi \vec{r} - (\vec{\omega}_{B/D}^B)^T P_p K \vec{\omega}_{B/D}^B - \alpha^2 \vec{q}_{D \rightarrow B}^T P_p K \vec{q}_{D \rightarrow B} \\
&\quad - 2\alpha \vec{q}_{D \rightarrow B}^T P_p K \vec{\omega}_{B/D}^B + \beta \vec{q}_{D \rightarrow B_p}^T \vec{\omega}_{B/D_p}^B \\
&= -\vec{r}^T P_p \Psi \vec{r} - (\vec{\omega}_{B/D_p}^B)^T K \vec{\omega}_{B/D_p}^B - \alpha^2 \vec{q}_{D \rightarrow B_p}^T K \vec{q}_{D \rightarrow B_p} \\
&\quad - 2\alpha \vec{q}_{D \rightarrow B_p}^T K \vec{\omega}_{B/D_p}^B + \beta \vec{q}_{D \rightarrow B_p}^T \vec{\omega}_{B/D_p}^B \\
&= -\vec{r}^T P_p \Psi \vec{r} - \vec{s}^T Q \vec{s}
\end{aligned} \tag{3.40}$$

where \vec{s} and Q are the augmented state vector and matrix represented in Eq. (3.41) and Eq. (3.42) respectively.

$$\vec{s} \equiv \begin{bmatrix} \vec{\omega}_{B/D_p}^B \\ q_{D \rightarrow B_p} \end{bmatrix} \tag{3.41}$$

$$Q \equiv \begin{bmatrix} K & \alpha K - (\beta/2) I_{3 \times 3} \\ \alpha K - (\beta/2) I_{3 \times 3} & \alpha^2 K \end{bmatrix} \tag{3.42}$$

If $Q > 0$, then $\dot{V}(\vec{x}) \leq 0$. To achieve this, the Schur complement of K in Q shown in Eq. (3.43) must be positive definite, $Q > 0 \iff S_Q > 0$.

$$S_Q = \alpha^2 K - \left(\alpha K - \frac{\beta}{2} I_{3 \times 3} \right)^T K^{-1} \left(\alpha K - \frac{\beta}{2} I_{3 \times 3} \right) \quad (3.43)$$

$$S_Q = \alpha^2 K - \alpha^2 K^T K^{-1} K + \alpha \beta K^T K^{-1} - \frac{\beta^2}{4} K^{-1}$$

Recall that K is a diagonal matrix, thus $K^T = K$.

$$S_Q = \alpha - \frac{\beta}{4} K^{-1} > 0$$

Therefore, the condition for $\dot{V}(\vec{x}) \leq 0$ is given by β satisfying the inequality in Eq. (3.44):

$$\beta < 4\alpha\underline{\lambda}(K) \quad (3.44)$$

where $\underline{\lambda}(K)$ denotes the minimum eigenvalue of the gain matrix K , corresponding to the smallest gain in its diagonal. Therefore, from Eq. (3.40), recalling Eq. (2.8) and the orthogonality of $P_g \perp P_p$, the final form of $\dot{V}(\vec{x})$ is shown in Eq. (3.45) if the condition in Eq. (3.44) is met.

$$\dot{V}(\vec{x}) = -\vec{r}_p^T \Psi \vec{r}_p - \vec{s}^T Q \vec{s} \leq 0 \quad \forall t \quad (3.45)$$

Here, $\dot{V}(\vec{x})$ is negative semidefinite due to the $\vec{r}_p^T \Psi \vec{r}_p$ term, which can lead to $\dot{V}(\vec{x}) = 0$ for values of $\tilde{\Theta} \neq \bar{\Theta}$. Therefore, it is required to extend the stability analysis via Barbalat's Lemma following the definition in **Section 2.2.5**.

3.2.2 Barbalat's Lemma for Asymptotic Stability Extension

$\dot{V}(\vec{x}) \leq 0$ allows to conclude the stability (i.e., boundedness) of the state vector \vec{x} . However, it does not allow the conclusion of the asymptotic stability of the signals. Therefore, Barbalat's Lemma is required to extend the stability analysis and conclude asymptotic stability of signals. This is to obtain the second time derivative of the Lyapunov function $\ddot{V}(\vec{x})$

and prove its boundedness.

$$\ddot{V}(\vec{x}) = -2\vec{r}_p^T \Psi \dot{\vec{r}}_p - \vec{r}_p^T \dot{\Psi} \vec{r}_p - 2\vec{s}^T Q \dot{\vec{s}} \quad (3.46)$$

where \vec{r}_p is Lyapunov bounded, and Ψ given in Eq. (3.31), is a function of $\hat{\Theta} = \vec{\Theta} - \tilde{\Theta}$, where $\vec{\Theta}$ is a constant and $\tilde{\Theta}$ is Lyapunov bounded. Furthermore, $\dot{\Psi}$ is also bounded as shown by its definition on Eq. (3.47).

$$\dot{\Psi} = \text{diag} \left(\dot{\hat{\Theta}}_p \odot \hat{\Theta}_p + \hat{\Theta}_p \odot \dot{\hat{\Theta}}_p \right) \quad (3.47)$$

where $\dot{\hat{\Theta}}_p$ is defined as in Eq. (3.48).

$$\dot{\hat{\Theta}}_p = \dot{P}_p \hat{\Theta} + P_p \dot{\hat{\Theta}} = \dot{P}_p \hat{\Theta} + P_p \gamma \Phi^T \vec{r} \quad (3.48)$$

where $\hat{\Theta}$ and Φ are bounded, \vec{r} is Lyapunov bounded, and γ is constant. Furthermore \dot{P}_p is also bounded as shown by Eq. (3.49) and Eq. (3.50).

$$\dot{P}_p = - \frac{\left[\dot{\vec{g}}^B (\vec{g}^B)^T + \vec{g}^B (\dot{\vec{g}}^B)^T \right] \|\vec{g}^B\|^2 - 2\vec{g}^B (\vec{g}^B)^T (\vec{g}^B) \dot{\vec{g}}^B}{\|\vec{g}^B\|^4} \quad (3.49)$$

$$\dot{\vec{g}}^B = -\frac{1}{2} \hat{\omega}_{B/I}^B \otimes \hat{q}_{I \rightarrow B}^* \otimes \hat{g}^I \otimes \hat{q}_{I \rightarrow B} + \frac{1}{2} \hat{q}_{I \rightarrow B}^* \otimes \hat{g}^I \otimes \hat{q}_{I \rightarrow B} \otimes \hat{\omega}_{B/I}^B \quad (3.50)$$

where both components of $\hat{\omega}_{B/I}^B = \hat{\omega}_{B/D}^B + \hat{\omega}_{D/I}^B$ are bounded by Lyapunov and design, respectively. Equally, both components of $\hat{q}_{I \rightarrow B} = \hat{q}_{I \rightarrow D}^* \otimes \hat{q}_{D \rightarrow B}$ are design and Lyapunov bounded, in that order. Finally, \hat{g}^I is a constant.

In order to show that $\dot{\vec{r}}_p$ and $\dot{\vec{s}}$ are bounded, it is required to show that both $\dot{\vec{q}}_{D \rightarrow B}$ and $\dot{\vec{\omega}}_{B/D}^B$ are bounded. Recalling their definition from **Section 2.2.1** and Eq. (3.27) respectively. Here, for $\dot{\vec{q}}_{D \rightarrow B} = \frac{1}{2} \alpha ((\vec{q}_{D \rightarrow B})^\times + q_{D \rightarrow B_0} I_{3 \times 3}) \vec{\omega}_{B/D}^B$, $\hat{q}_{D \rightarrow B}$ and $\vec{\omega}_{B/D}^B$ are both Lyapunov bounded. On the other hand, if the controller obtained defined in Eq. (3.29) is plugged into

Eq. (3.27).

$$\begin{aligned} J^B \dot{\vec{\omega}}_{B/D}^B = & P_g \left[-\dot{j}_m^B \vec{\omega}_{B/I}^B - \vec{\omega}_{B/I}^B \times J^B \vec{\omega}_{B/I}^B \right] + \Phi \vec{\Theta} - P_p \Phi \hat{\Theta} \\ & - P_g J^B \left[\dot{\vec{\omega}}_{D/I}^B + (\vec{\omega}_{D/I}^B \times \vec{\omega}_{B/D}^B) \right] - P_p \left(K + \Psi + \frac{1}{2} j_m^B \right) \vec{r} \end{aligned} \quad (3.51)$$

where J^B and \dot{j}_m^B are bounded; Φ , P_p and P_g are all functions of $\hat{q}_{D \rightarrow B}$ and \vec{g}^I , which are Lyapunov bounded and constant respectively. Furthermore, $\vec{\Theta}$ and K are constants, $\hat{\Theta}$ and Ψ are bounded, $\vec{\omega}_{D/I}^B$ and $\dot{\vec{\omega}}_{D/I}^B$ are bounded by design, and $\vec{\omega}_{B/I}^B = \vec{\omega}_{B/D}^B + \vec{\omega}_{D/I}^B$ which are Lyapunov bounded and design bounded respectively.

Finally, because $V(\vec{x}) = \frac{1}{2} \vec{r}^T J^B \vec{r} + \frac{1}{2} \gamma^{-1} \tilde{\Theta}^T \tilde{\Theta} + \beta [\vec{q}_{D \rightarrow B}^T \vec{q}_{D \rightarrow B} + (q_{D \rightarrow B_0} - 1)^2] > 0$, $\dot{V}(\vec{x}) = -\vec{r}_p^T \Psi \vec{r}_p - \vec{s}^T Q \vec{s} \leq 0$, and $\ddot{V}(\vec{x}) = -2\vec{r}_p^T \Psi \dot{\vec{r}}_p - \vec{r}_p^T \Psi \vec{r}_p - 2\vec{s}^T Q \dot{\vec{s}}$ is bounded. It can be concluded that:

$$\begin{aligned} \lim_{t \rightarrow \infty} \vec{\omega}_{B/D_p}^B &= \vec{0} \\ \lim_{t \rightarrow \infty} \vec{q}_{D \rightarrow B_p} &= \vec{0} \end{aligned} \quad (3.52)$$

This means the components on the plane perpendicular to the gravity vector will be controllable. The components parallel to the gravity vector will be $\vec{\omega}_{B/D_g}^B = \vec{q}_{D \rightarrow B_g} = \vec{0}$ as per design of the D frame trajectory.

3.3 Parameter Convergence

As shown in **Section 3.2.2**, Eq. (3.52), it has been demonstrated that the components orthogonal to the gravitational vector will converge to zero as time goes to infinity for the angular rates and attitude of the B frame with respect to the D frame. This section demonstrates how the asymptotic stability results of the state vector, combined with the design of the desired trajectory shown in **Section 3.1.4** lead to asymptotic stability of all the components of the estimation vector to the real values.

Recalling Eq. (3.30), and applying the results from Eq. (3.52), the following statement

holds:

$$\begin{aligned}
\lim_{t \rightarrow \infty} \dot{\hat{\Theta}} &= \lim_{t \rightarrow \infty} \gamma \Phi^T \vec{r} \\
&= \lim_{t \rightarrow \infty} \gamma \Phi^T (\vec{r}_p + \vec{r}_g) \\
&= \lim_{t \rightarrow \infty} \gamma \Phi^T \vec{r}_p \\
&= \vec{0}
\end{aligned} \tag{3.53}$$

Therefore, the following is true for the limit of the estimation vector as time goes to infinity:

$$\lim_{t \rightarrow \infty} \hat{\Theta} = \vec{C} \tag{3.54}$$

where \vec{C} is an arbitrary constant value. Furthermore, recalling Eq. (3.29), and applying its limit as time goes to infinity:

$$\lim_{t \rightarrow \infty} \vec{u} = -\Phi \vec{C} \tag{3.55}$$

Recall that for $t < T_1$, the desired dynamics are defined as in Eq. (3.17). This results in the alignment of the D and I z-axis frames. Therefore, as $\vec{\omega}_{B/D_p}^B$ and $\vec{q}_{D \rightarrow B_p}$ converge asymptotically to zero, the B z-axis will converge to the D z-axis, which itself is equal to the I z-axis. The stabilized attitude before T_1 is represented in Figure 3.3, note that the z and y axes of B and I frame are not aligned after stabilization at all time, due to the constant uncontrollable spin about the z-axis. However, after stabilization, the B xy-plane is aligned with the I xy-plane at all times before T_1 . Because convergence of $\vec{\omega}_{B/D_p}^B$ has been proven in Eq. (3.52) the following statement also holds:

$$\lim_{t \rightarrow \infty} \dot{\vec{\omega}}_{B/D}^B = \vec{0} \tag{3.56}$$

On the other hand, taking the limit as time approaches infinity of the right hand side of

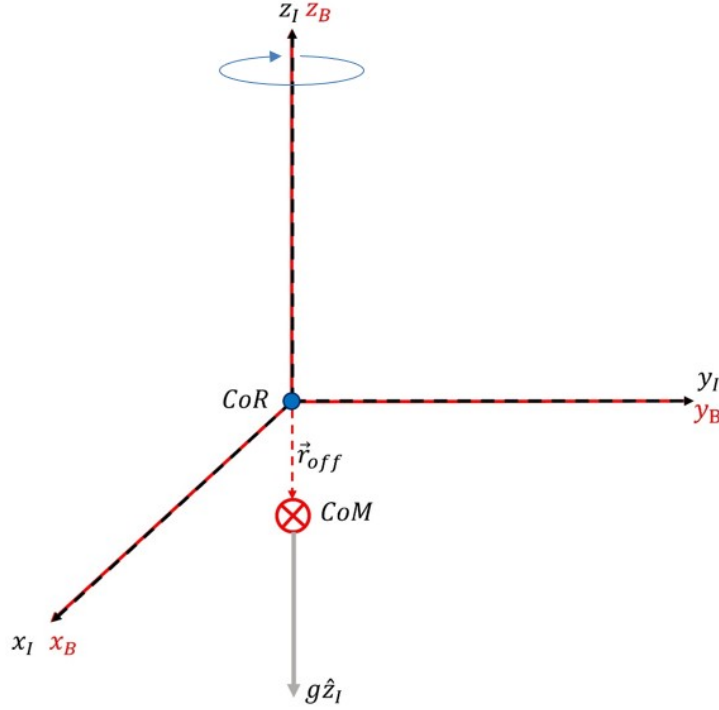


Figure 3.3 Visualization of stabilized B frame with respect to I frame before T_1 .

Eq. (3.28), the following is obtained:

$$\lim_{t \rightarrow \infty} J^B \dot{\omega}_{B/D}^B = \Phi \vec{\Theta} - \vec{u} \quad (3.57)$$

Plugging in the limit of the control input found in Eq. (3.55), as well as the known limit in Eq. (3.56), the following equality is obtained:

$$\begin{aligned}
\vec{0} &= \Phi (\vec{\Theta} - \vec{C}) \\
&= -Mg \begin{bmatrix} 0 & -1 & 0 \\ 1 & 0 & 0 \\ 0 & 0 & 0 \end{bmatrix} (\vec{\Theta} - \vec{C}) \\
&= -Mg \begin{bmatrix} C_2 - \Theta_2 \\ \Theta_1 - C_1 \\ 0 \end{bmatrix}
\end{aligned} \quad (3.58)$$

Because M and g are both known constant values, the following must be true: $C_1 = \Theta_1$ and $C_2 = \Theta_2$, such that:

$$\begin{aligned}\lim_{t \rightarrow \infty} \tilde{\Theta}_1 &= 0 \\ \lim_{t \rightarrow \infty} \tilde{\Theta}_2 &= 0\end{aligned}\tag{3.59}$$

The same procedure can be used to prove the convergence of the z component of the estimation error to zero. After T_2 , the asymptotic stability to the equilibrium point, will lead to the B frame xy-plane to be at an offset angle ψ with respect to the I xy-plane, while the B y-axis will maintain alignment with the I xy-plane, as displayed in Figure 3.4.

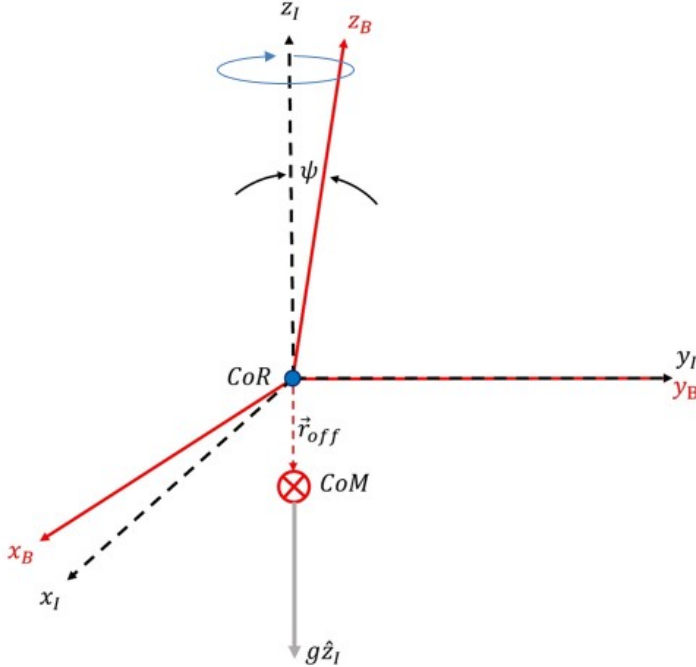


Figure 3.4 Visualization of stabilized B frame with respect to I frame after T_2 .

In this case, the first two components of the estimation error have been proven to converge to zero. After convergence, the update law for the estimates that have converged to their true values is stopped by setting the first two learning rates to zero. With the new desired

attitude and angular rates for $t > T_2$, the limit of Φ as time goes to infinity becomes:

$$\lim_{t \rightarrow \infty} \Phi = -Mg \begin{bmatrix} 0 & -\cos(\psi) & 0 \\ \cos(\psi) & 0 & -\sin(\psi) \\ 0 & \sin(\psi) & 0 \end{bmatrix} \quad (3.60)$$

Such that Eq. (3.58) can be rewritten as:

$$\begin{aligned} \vec{\theta} &= \Phi (\vec{\Theta} - \vec{C}) \\ &= -Mg \begin{bmatrix} 0 & -\cos(\psi) & 0 \\ \cos(\psi) & 0 & -\sin(\psi) \\ 0 & \sin(\psi) & 0 \end{bmatrix} (\vec{\Theta} - \vec{C}) \\ &= -Mg \begin{bmatrix} (C_2 - \Theta_2) \cos(\psi) \\ (C_1 - \Theta_1) \cos(\psi) + (\Theta_3 - C_3) \sin(\psi) \\ (\Theta_2 - C_2) \sin(\psi) \end{bmatrix} \end{aligned} \quad (3.61)$$

Recalling the results from $t < T_1$ displayed in Eq. (3.59), where $C_1 = \Theta_1$ and $C_2 = \Theta_2$, Eq. (3.61) becomes:

$$\vec{\theta} = \begin{bmatrix} 0 \\ -Mg(\Theta_3 - C_3) \sin(\psi) \\ 0 \end{bmatrix} \quad (3.62)$$

Because, M , g , and ψ are known constant values, one can conclude that for Eq. (3.62) to hold, $C_3 = \Theta_3$, such that the following can be concluded:

$$\lim_{t \rightarrow \infty} \tilde{\Theta}_3 = 0 \quad (3.63)$$

3.4 Sliding Mass Control

It has been stated in **Section 3.1.1** that the input torque is generated as a function of the position of the sliding masses, as shown in Eq. (3.14). This means that the real control

input that must be commanded to the system is the sliding mass position $\vec{\sigma}$. However, as stated by Chesi et al. in [9], the skew symmetric matrix obtained from the gravity vector is by definition singular. To solve for $\vec{\sigma}$, Eq. (3.64) has been borrowed from [9]. Because the designed control has been defined to only act in the plane perpendicular to the gravity vector, Eq. (3.64) will always have a solution for $\vec{\sigma}$, as demonstrated in [9].

$$\vec{\sigma} = \frac{\vec{g}^B \times \vec{u}}{||\vec{g}^B||^2 m} \quad (3.64)$$

4 Numerical Simulations

The dynamics of the system presented in **Section 3.1** with the designed adaptive control and update laws designed in **Section 3.2** have been verified in a simulation environment using MATLAB R2023b. The simulations used a Runge-Kutta fourth-order integrator with $dt = 0.001s$ fixed-step and propagated for $T = 300s$. The physical parameters used in the simulations are obtained from the 5-DOF testbed currently under manufacturing and assembly process in the ADvanced Autonomous Multiple Spacecraft (ADAMUS) laboratory at Embry-Riddle Aeronautical University (ERAU). The inertia matrix of the 5-DOF testbed has been obtained using a high-fidelity *CAD* model of the 5-DOF testbed.

The *CoM* to *CoR* initial offset used in the simulation is $\vec{\Theta} = [0.9 \ -1.2 \ 1.7]^T mm$, with a total mass of the testbed of $M = 4.2 kg$, and sliding masses $m_1 = m_2 = m_3 = 0.3 kg$. The initial *MoI* of the testbed has been selected as $J_0^B = \text{diag}([0.226 \ 0.257 \ 0.266]) kgm^2$. The initial conditions for the simulation are $\vec{\omega}_{B/I}^B(t_0) = [0.0888 \ 0.08229 \ 0.13611]^T rad/s$ and $\hat{q}_{I \rightarrow B}(t_0) = \hat{1}$ for angular rates and attitude quaternion of the *B* frame respectively. The initial estimates for the *CoM* offset are $\hat{\Theta}(t_0) = \vec{0}$.

Recalling the control and update laws in Eq. (3.29) and Eq. (3.30). The control gains K and α , and the learning rate γ has been selected as presented in Eq. (4.1) thru Eq. (4.3).

$$K = \begin{cases} (10^{-3})I_{3 \times 3}, & \text{if } t \leq T_1 \\ (8 \times 10^{-4})I_{3 \times 3}, & \text{otherwise} \end{cases} \quad (4.1)$$

$$\alpha = 3I_{3 \times 3} \quad (4.2)$$

$$\gamma = \begin{cases} (3 \times 10^{-5})I_{3 \times 3}, & \text{if } t \leq T_1 \\ (2 \times 10^{-4})\text{diag}([0 \ 0 \ 1]), & \text{otherwise} \end{cases} \quad (4.3)$$

Where $T_1 = 50s$ is defined as the time at which $\vec{\omega}_{B/D_p}^B$, $\vec{q}_{D \rightarrow B_p}$ and $\tilde{\Theta}_p$ converge to zero. At T_1 , the desired trajectory begins the impulsive maneuver, recalling from Eq. (3.20), an

angle error between the D and I frames xy-planes is $\psi = \pi/9$, which leads to an impulsive maneuver defined as in Eq. (4.4).

$$\omega_{D/I_e}^D = \frac{\pi^2}{12(T_2 - T_1)} \sin\left(\frac{\pi}{T_2 - T_1}(t - T_1)\right) \quad \forall \quad t \in \{T_1, T_2\} \quad (4.4)$$

Where the end time of the impulsive maneuver has been selected to be $T_2 = 80s$ for a total impulsive maneuver time of $\Delta T_e = 30s$.

5 Results & Discussion

This chapter presents and discusses the results obtained from the numerical simulation setup in described in **Chapter 4**.

5.1 Desired Trajectory Results

First, the results of the numerical simulation for the trajectory of the D frame are presented. Figure 5.1 displays the angular rates of the D frame with respect to the I as designed in **Section 3.1.4**.

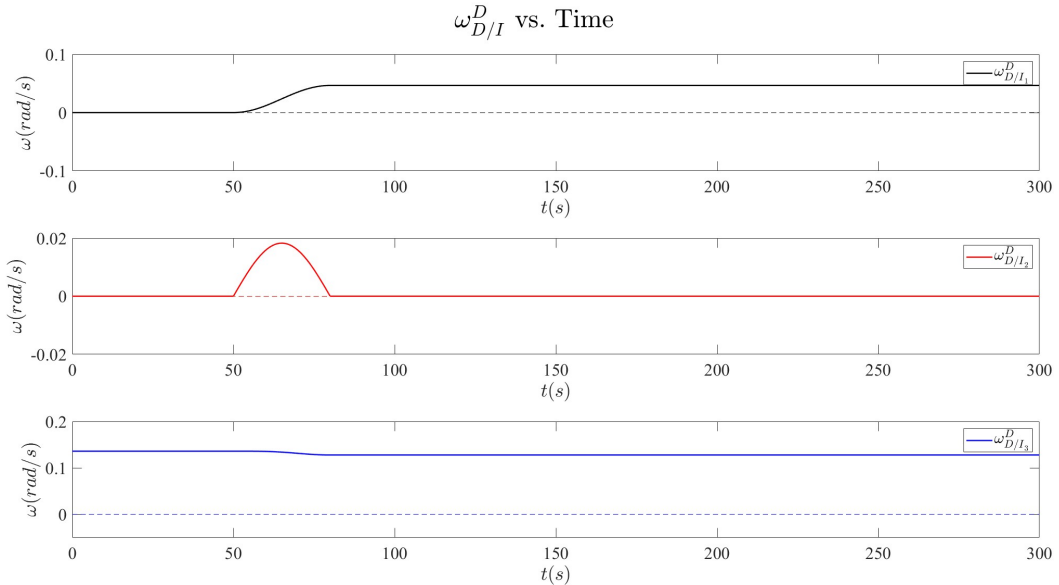


Figure 5.1 Simulation results for angular rates of the D frame with respect to the I frame in the I frame $\vec{\omega}_{D/I}^I$ as a function of time.

Note that as expected, for $t < T_1 = 50s$, the D frame is spinning purely about its z-axis. Then, for the interval $T_1 \leq t \leq T_2 = 80s$, the D frame begins the impulsive maneuver, which corresponds in a sinusoidal impulsive on the about the D frame y-axis, which starts and ends at $\omega_{D/I_y}^D = 0$. Then, for $t > T_2$ the impulsive maneuver continues the constant to spin about the inertial z-axis, and as expected this results on constant angular rates about the I x and z-axes.

The attitude results are also relevant to understand how the testbed should behave. Figure 5.2 displays the attitude quaternion of the D frame with respect to the I frame as a

function of time. The behavior of the four quaternion components are displayed, where the scalar component of the quaternion is shown in black, and the vector quaternion components in red, blue, and green. This color scheme is constant throughout all plots representing attitude quaternions.

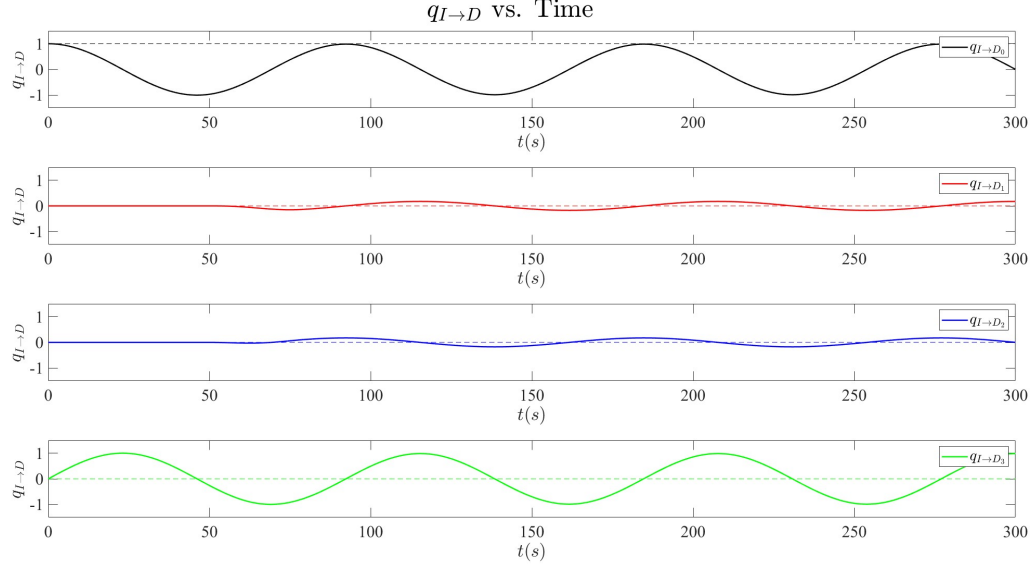


Figure 5.2 Simulation results for the attitude of the D frame with respect to the I frame $\hat{q}_{I \rightarrow D}$ as a function of time.

It can be observed that for $t < T_1$, the attitude quaternion shows pure spin of the D frame while maintaining alignment of the D and I frames z-axes. The impulsive maneuver defined in the angular rates of the D frame from the interval $T_1 \leq t \leq T_2$ affects the attitude of the D frame. After $t > T_2$, from the results of $q_{I \rightarrow D}$, it can be seen that the desired ψ is obtained, and remains constant.

5.2 Controlled System Results

In **Section 5.1**, it has been shown that the desired trajectory behaves as expected by design. This section focuses on the numerical simulation results of the controlled system tracking the desired trajectory. Recalling, the stability proof in **Section 3.2**, the state vector \vec{x} must converge to the desired equilibrium point. This is shown to be true for $\vec{\omega}_{B/D}^B$ in Figure 5.3 thru Figure 5.5.

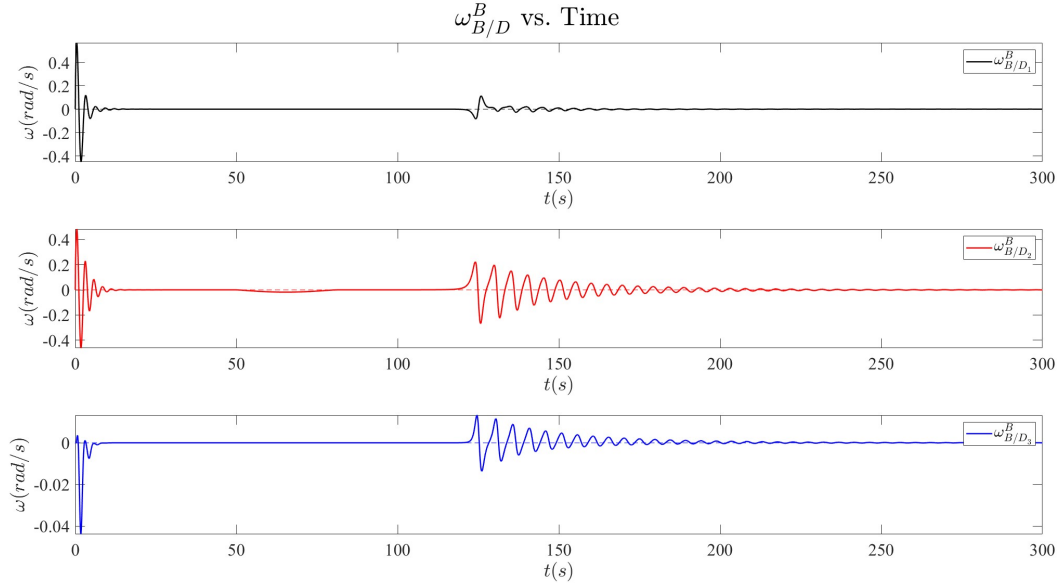


Figure 5.3 Simulation results for angular rates of the B frame with respect to the D frame in the B frame $\vec{\omega}_{B/D}^B$ as a function of time.

It can be observed in Figure 5.3 that the angular rates of the B frame with respect to the D frame converge to zero before and after the excitation period $T_1 \leq t \leq T_2$.

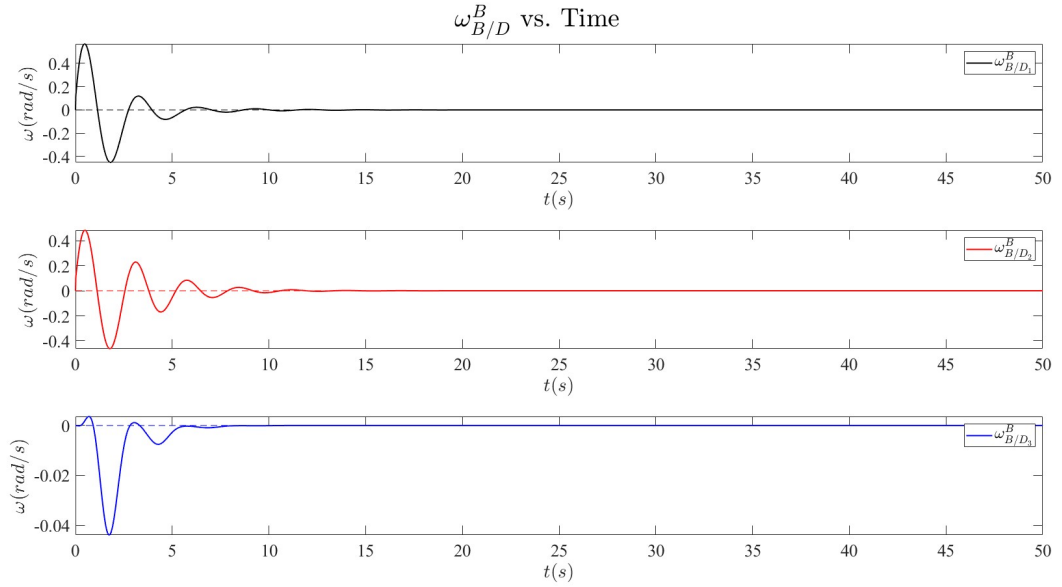


Figure 5.4 Simulation results for angular rates of the B frame with respect to the D frame in the B frame $\vec{\omega}_{B/D}^B$ as a function of time, close up from 0 to 50 seconds.

Figure 5.4 focuses on the pre-excitation period to better present the transient behavior of the system. It can be seen that all values of $\vec{\omega}_{B/D}^B$ converge to zero after 20 seconds, exhibiting an oscillatory transient response for the initial 10 seconds. This transient response is to be expected from the uncontrolled behavior of the system.

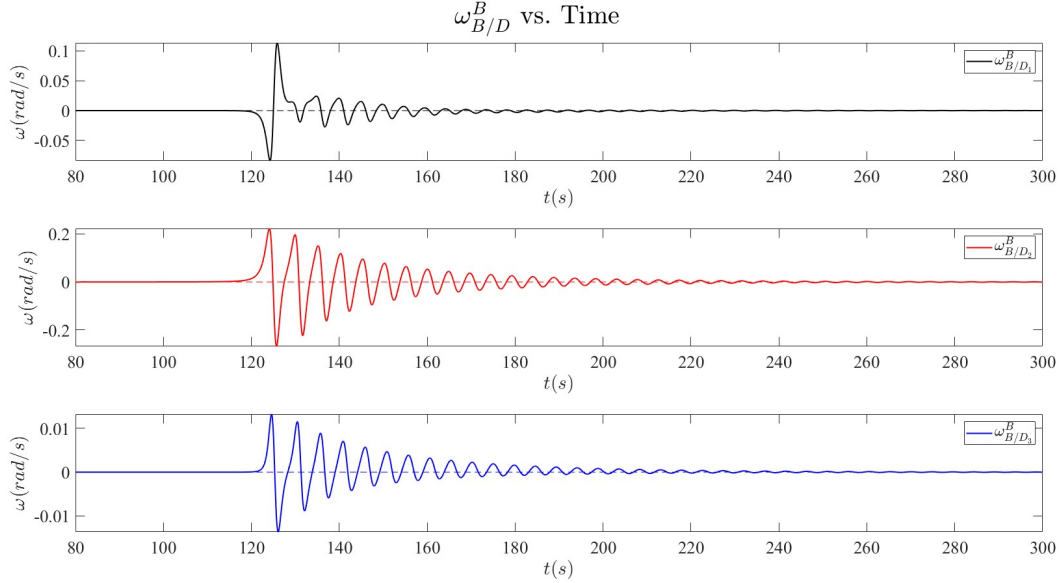


Figure 5.5 Simulation results for angular rates of the B frame with respect to the D frame in the B frame $\vec{\omega}_{B/D}^B$ as a function of time, close up from 80 to 300 seconds.

Figure 5.5 displays the angular rates of the system post-excitation. Once again, it can be seen that the system presents an oscillatory response. However, in this case the settling time is larger, having the states converge to zero at 280 seconds. It is important to note, that although the excitation maneuver begins at $t = 50s$, this is not reflected high angular rate errors until $t = 120s$, this is due to the estimation errors compensating for the new conditions during that time period, as will be seen in Figure 5.12. Nonetheless, the excitation maneuver can be slightly observed in the second subplot of Figure 5.3. With these results the stability proof in terms of angular rates is supported by the numerical simulation environment.

Similarly Figure 5.6 thru Figure 5.8 present the attitude of the B frame with respect to the D frame.

As with the angular rates error of the system, the quaternion error between B and D

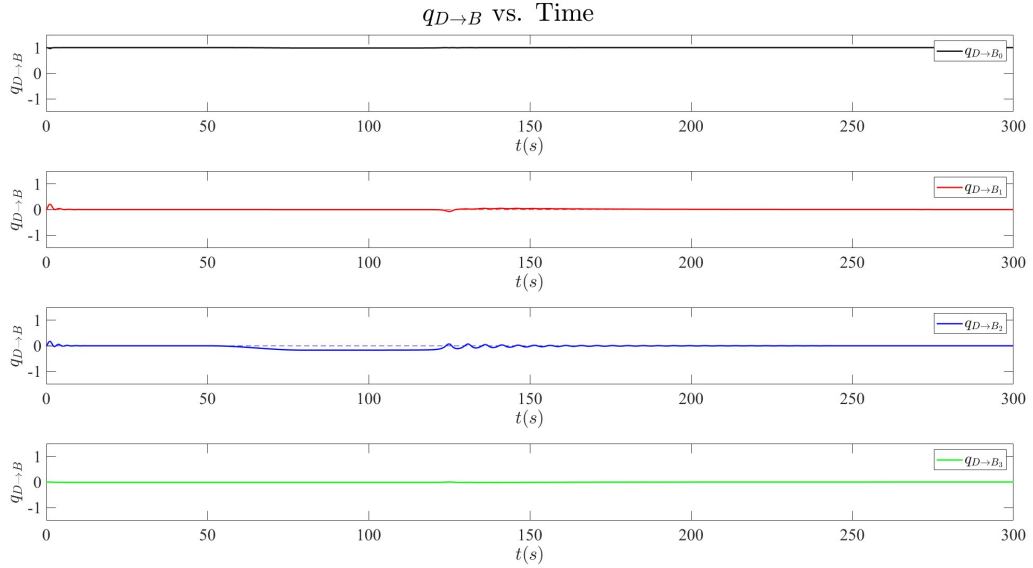


Figure 5.6 Simulation results for the attitude of the B frame with respect to the D frame $\hat{q}_{D \rightarrow B}$ as a function of time.

frames converges to zero. Recall, that the stability proof included restrictions dependent on the desired trajectory. This can be clearly seen in the plot above, where it can be seen that $q_{D \rightarrow B_3}$ trajectory shown in green never leaves the equilibrium point. Therefore, it is shown that the assumption on the stability proof is true with this design of reference trajectory.

Taking a closer look into the transient behavior of the system in terms of the quaternion, an oscillatory response can be observed for the first 10 seconds of the pre-excitation period in Figure 5.7. On the other hand, referring to Figure 5.8 for the behavior of the system during and after the excitation maneuver. It can be clearly noticed that there is an error on $q_{D \rightarrow B_2}$ to be expected as the excitement rotation maneuver is being made about the y-axis of the D frame. In this case, the system totally converges to the desired attitude after excitation at 200 seconds.

Figure 5.9 displays the behavior of the system with respect to the I frame in the B frame. Although these results do not give further insight on stability, they show how the B frame exhibits equal behavior to the D frame after convergence of the state parameters.

Another relevant result is presented in Figure 5.10 and Figure 5.11, which represent the

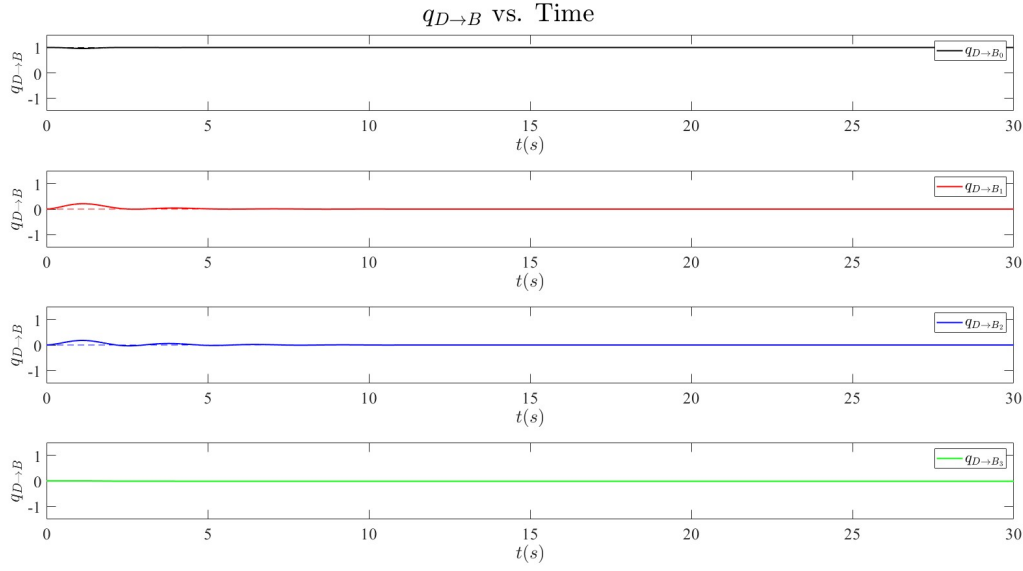


Figure 5.7 Simulation results for the attitude of the B frame with respect to the D frame $\hat{q}_{D \rightarrow B}$ as a function of time, close up from 0 to 30 seconds.

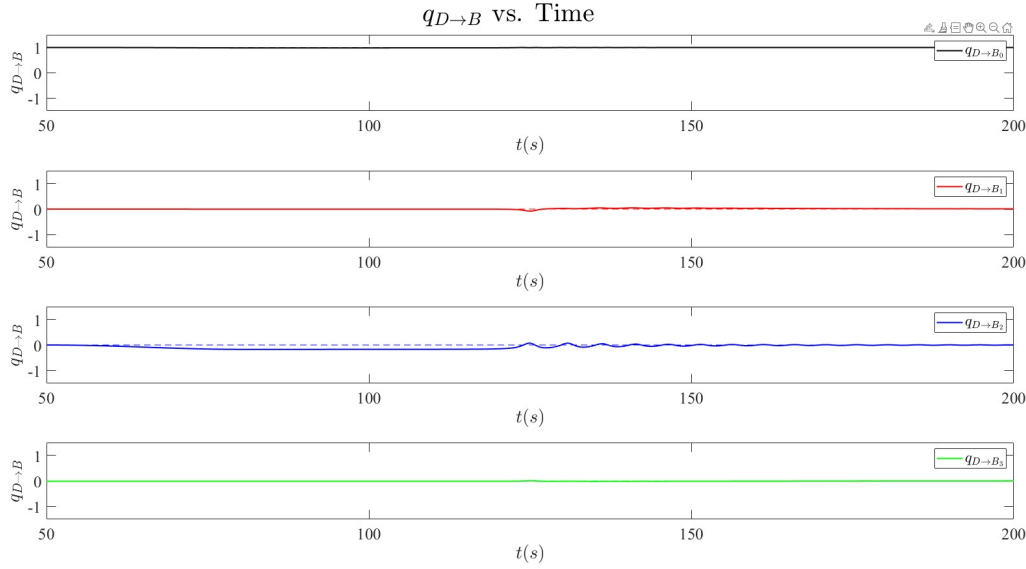


Figure 5.8 Simulation results for the attitude of the B frame with respect to the D frame $\hat{q}_{D \rightarrow B}$ as a function of time, , close up from 50 to 200 seconds.

behavior of the system as observed in the I frame. As shown in **Section 3.1**, the system has no control authority along the inertial z-axis, this means that the angular velocity of the body about the z-axis of the I frame is expected to remain constant. For this reason,

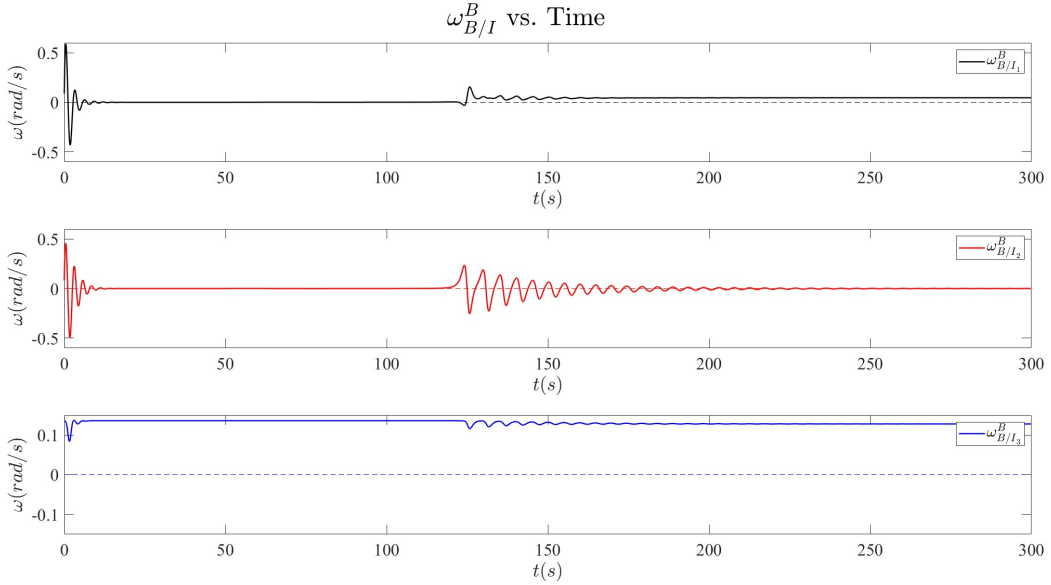


Figure 5.9 Simulation results for angular rates of the B frame with respect to the I frame in the B frame $\vec{\omega}_{B/I}^B$ as a function of time.

in **Section 3.2** the control law has been designed using the projection operator to ensure that no torques will be required to obtain asymptotic stability of the equilibrium points of the system.

The results from Figure 5.10 show that, in fact, the system does not attempt to control the inertial z-axis angular rate, which remains constant during the entirety of the simulation. Furthermore, analyzing the behavior of $q_{I \rightarrow B_3}$ in Figure 5.11, it can be observed that it produces a continuous sinusoidal that is not perturbed for the entirety of the simulation. This validates that the control objective is achieved for the under-actuated system representing the 5-DOF testbed.

5.3 Estimation Results

This section displays the convergence of the estimated *CoM* to *CoR* offset $\hat{\Theta}$. The results of the simulation for these parameters are displayed in Figure 5.12 in terms of the estimation error $\tilde{\Theta}$.

The estimation errors $\tilde{\Theta}$ are shown to converge to zero in all three axis. It can be observed that fast estimation is obtained for $\tilde{\Theta}_1$ and $\tilde{\Theta}_2$ aligned to the x and y axes of the B frame.

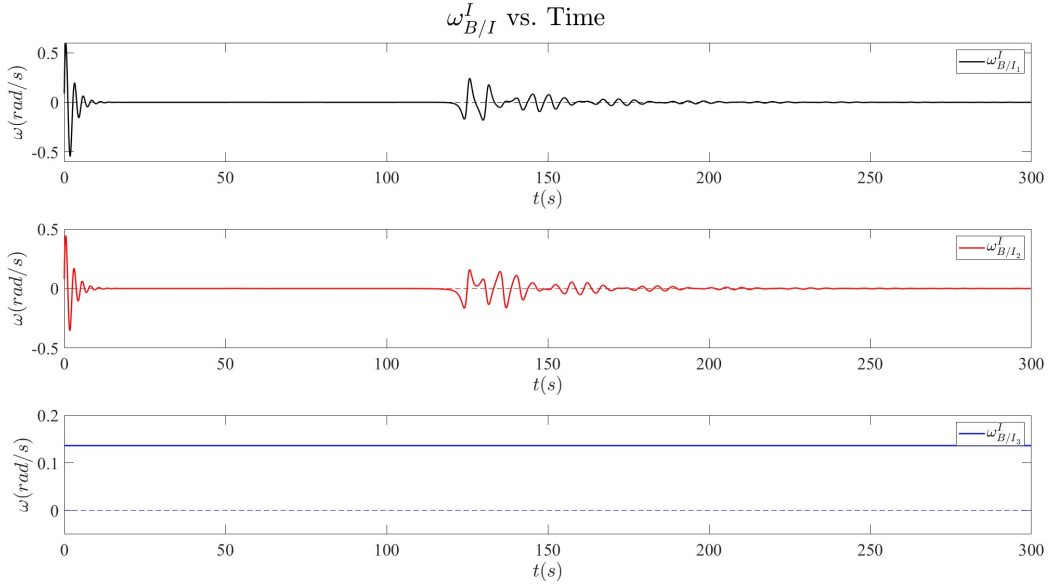


Figure 5.10 Simulation results for angular rates of the B frame with respect to the I frame in the I frame $\vec{\omega}_{B/I}^I$ as a function of time.

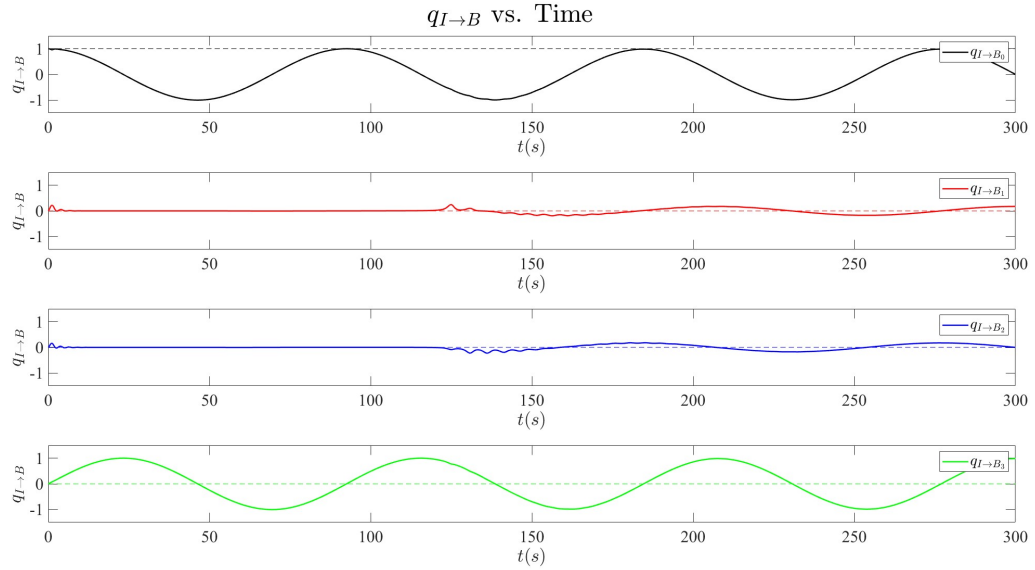


Figure 5.11 Simulation results for the attitude of the B frame with respect to the I frame $\hat{q}_{I \rightarrow B}$ as a function of time.

This can be better observed in Figure 5.13. Then, after T_1 , the estimation of the third axis offset $\hat{\Theta}_3$ begins its convergence to the true value. The transient behavior of $\tilde{\Theta}_3$ is more oscillatory than the other two estimates, and it also has a larger settling time. Nonetheless,

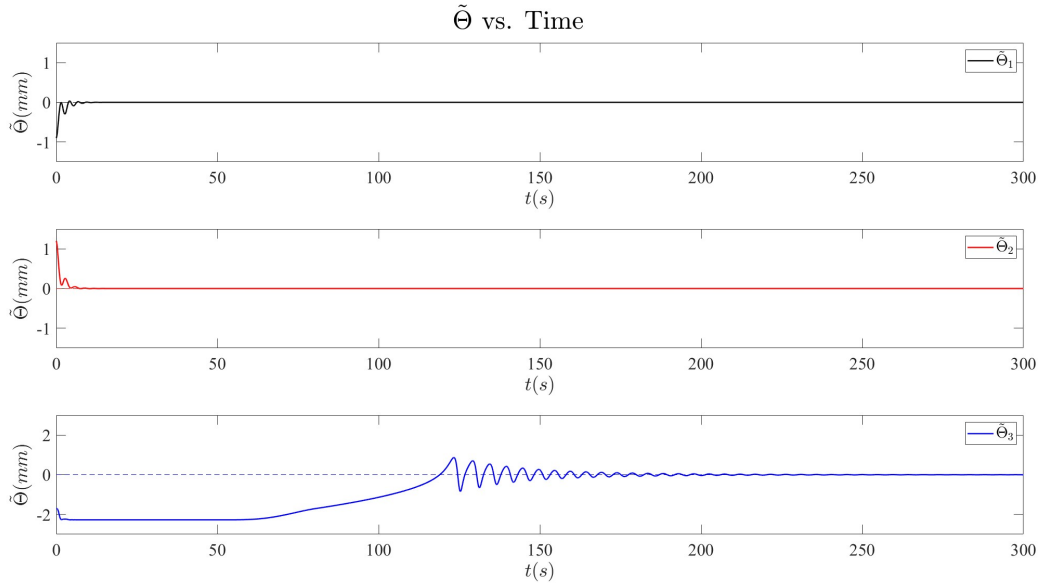


Figure 5.12 Simulation results for estimation errors $\tilde{\Theta}$ as a function of time.

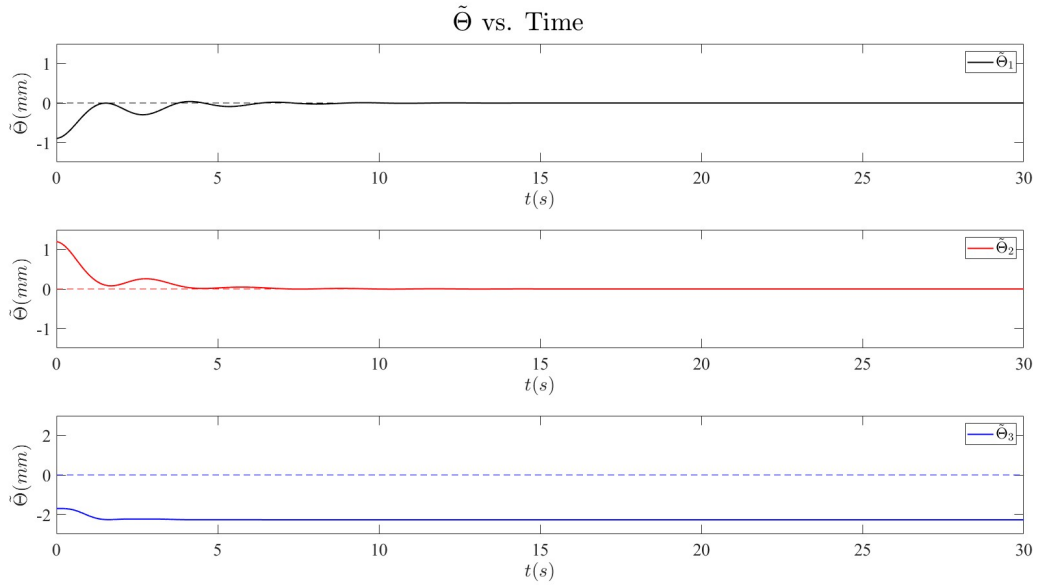


Figure 5.13 Simulation results for estimation errors $\tilde{\Theta}$ as a function of time, close up from 0 to 30 seconds.

all estimates converge to their true values at $t = 250s$ after the excitation maneuver is performed.

5.4 Sliding Mass Position Results

The final result presented in this work is the position of the masses, obtained by solving for σ as demonstrated in Eq. (3.64). Figure 5.14 displays the sliding mass position as the system follows the desired trajectory.

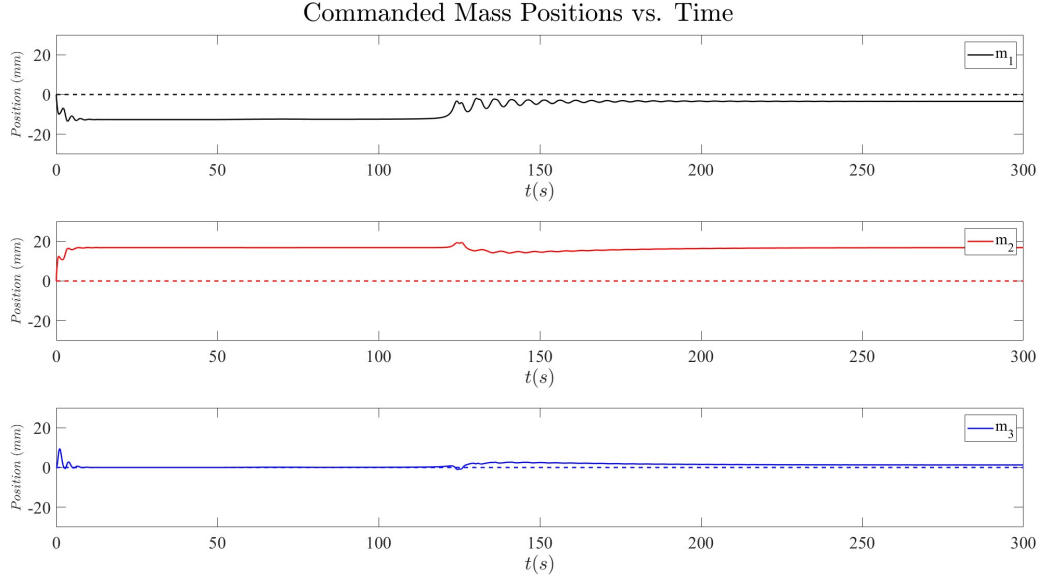


Figure 5.14 Simulation results commanded positions of the sliding masses $\vec{\sigma}$ as a function of time.

Although these results are obtained from the numerical simulation environment it is still important to ensure that the designed adaptive controller does not drive the masses to non reachable positions. As it can be observed from the results presented above, the sliding mass positions required to produce the desired torque do not displace more than 20 millimeters, which is great to notice, as the designs of these types of testbeds usually aim to be light and compact. As stated on *Chapter 4*, the parameters used in this simulation are based on a current design being assembled at Embry-Riddle Aeronautical University. Therefore, expecting this simulation results to reflect the experimental validation to be completed in a the future.

6 Conclusions & Future Work

In this work, a model for a spacecraft testbed with three rotational degrees of freedom with unknown *CoM* to *CoR* has been presented, including time-varying moment of inertia due to the effects of the sliding masses. A model reference adaptive controller and estimation law have been derived, which ensure asymptotic convergence of the system states to the desired model states, as well as convergence of the estimates to their true values. Through Lyapunov stability theory, the system's desired equilibrium points have been proven to be stable. Then, using Barbalat's Lemma, the conclusion of stability has been extended to ensure asymptotic convergence of the system states to the equilibrium point.

The controller has been designed in terms of the under actuated system, to ensure that the input torques can be obtained from the gravity torque effects due to the positioning of the sliding masses. Therefore, an adaptive control and estimation laws that utilize *MMC* only have been demonstrated. Furthermore, the stability proof has been improved with respect to previous state-of-the-art controllers.

The adaptive control and estimation laws have been validated in a numerical simulation environment using a Runge-Kutta fourth order integration method. The numerical simulation environment has confirmed that the system states are driven by the control and estimation laws to the desired values. Furthermore, it has been confirmed that the reference model enables the assumptions made in the Lyapunov analysis. The numerical simulation results have also demonstrated that the control input can be obtained with *MMC* only, and that the commanded positions of the system do not exceed actuator limitations.

In the future, this work will be validated using a 5-*DOF* spacecraft simulator currently under assembly at the ADAMUS Laboratory at Embry-Riddle Aeronautical University. Furthermore, this work assumes that the initial moment of inertia of the testbed is known. An extension of this work to include unknown time-varying moment of inertia will be beneficial to increase robustness. Although this research allows tuning of the control gains and estimation update laws to ensure that the sliding masses do not exceed physical limitations

in terms of position and velocity, an extension including actuator dynamics would be an improvement in robustness of the system.

The basis of this work can be used for estimation of unknown *CoM* for spacecraft under the effects of gravity gradient in Low Earth Orbit (*LEO*) using only *MMC*. Attitude control of spacecraft utilizing *MMC* has been shown in [21, 22], and methods estimation of unknown *CoM* are present in the literature in [23, 24]. However, the author has found no work reported in the literature of estimation of *CoM* on spacecraft using only *MMC* under gravity gradient disturbance in *LEO*. For this reason, this would be a feasible route to extend this work into the space environment.

REFERENCES

- [1] Xu, Z., Qi, N., and Chen, Y., “Parameter estimation of a three-axis spacecraft simulator using recursive least-squares approach with tracking differentiator and Extended Kalman Filter,” *Acta Astronautica*, Vol. 117, 2015, pp. 254–262. <https://doi.org/https://doi.org/10.1016/j.actaastro.2015.08.010>, URL <https://www.sciencedirect.com/science/article/pii/S0094576515003264>.
- [2] Sharifi, G., Mirshams, M., and Ousaloo, H. S., “Mass properties identification and automatic mass balancing system for satellite attitude dynamics simulator,” *Proceedings of the Institution of Mechanical Engineers, Part G: Journal of Aerospace Engineering*, Vol. 233, No. 3, 2019, pp. 896–907. <https://doi.org/10.1177/0954410017742932>, URL <https://doi.org/10.1177/0954410017742932>.
- [3] Saulnier, K., Pérez, D., Huang, R., Gallardo, D., Tilton, G., and Bevilacqua, R., “A six-degree-of-freedom hardware-in-the-loop simulator for small spacecraft,” *Acta Astronautica*, Vol. 105, 2014. <https://doi.org/10.1016/j.actaastro.2014.10.027>.
- [4] da Silva, R. C., Borges, R. A., Battistini, S., and Cappelletti, C., “A review of balancing methods for satellite simulators,” *Acta Astronautica*, Vol. 187, 2021, pp. 537–545. <https://doi.org/https://doi.org/10.1016/j.actaastro.2021.05.037>, URL <https://www.sciencedirect.com/science/article/pii/S0094576521002745>.
- [5] da Silva, R. C., Guimarães, F. C., de Loiola, J. V. L., Borges, R. A., Battistini, S., and Cappelletti, C., “Tabletop Testbed for Attitude Determination and Control of Nanosatellites,” *Journal of Aerospace Engineering*, Vol. 32, No. 1, 2019, p. 04018122. [https://doi.org/10.1061/\(ASCE\)AS.1943-5525.0000952](https://doi.org/10.1061/(ASCE)AS.1943-5525.0000952), URL <https://ascelibrary.org/doi/abs/10.1061/%28ASCE%29AS.1943-5525.0000952>.
- [6] Levenberg, K., “A METHOD FOR THE SOLUTION OF CERTAIN NON – LINEAR

- PROBLEMS IN LEAST SQUARES,” *Quarterly of Applied Mathematics*, Vol. 2, 1944, pp. 164–168. URL <https://api.semanticscholar.org/CorpusID:124308544>.
- [7] da Silva, R. C., “FILTERING AND ADAPTIVE CONTROL FOR BALANCING A NANOSATELLITE TESTBED,” Master’s thesis, UNIVERSITY OF BRASILIA, 2018.
- [8] Kim, J. J., and Agrawal, B. N., “Automatic Mass Balancing of Air-Bearing-Based Three-Axis Rotational Spacecraft Simulator,” *Journal of Guidance, Control, and Dynamics*, Vol. 32, No. 3, 2009, pp. 1005–1017. <https://doi.org/10.2514/1.34437>, URL <https://doi.org/10.2514/1.34437>.
- [9] Chesi, S., Gong, Q., Pellegrini, V., Cristi, R., and Romano, M., “Automatic Mass Balancing of a Spacecraft Three-Axis Simulator: Analysis and Experimentation,” *Journal of Guidance, Control, and Dynamics*, Vol. 37, No. 1, 2014, pp. 197–206. <https://doi.org/10.2514/1.60380>.
- [10] Xuan, H. T., Chemori, A., Anh, T. P., Le Xuan, H., Hoai, T. P., and Viet, P. V., “From PID to L1 adaptive control for automatic balancing of a spacecraft three-axis simulator,” *Int. J. Emerg. Technol. Adv. Eng.*, Vol. 6, No. 1, 2016, pp. 77–86.
- [11] Hua, B., Chen, L., Wu, Y., and Chen, Z., “A study of PID and L1 adaptive control for automatic balancing of a spacecraft three-axis simulator,” *International Journal of Intelligent Computing and Cybernetics*, Vol. 11, No. 2, 2018, pp. 269–284.
- [12] Bahu, A., and Modenini, D., “Automatic mass balancing system for a dynamic CubeSat attitude simulator: development and experimental validation,” *CEAS Space Journal*, Vol. 12, No. 4, 2020, pp. 597–611. <https://doi.org/10.1007/s12567-020-00309-5>, URL <https://doi.org/10.1007/s12567-020-00309-5>.
- [13] Lavretsky, E., and Wise, K. A., *Robust and Adaptive Control with Aerospace Applications*, Springer, 2013.

- [14] Junkins, J. L., and Schaub, H., *Analytical Mechanics of Space Systems Second Edition*, AIAA, 2009.
- [15] Gui, H., and Vukovich, G., “Dual-quaternion-based adaptive motion tracking of space-craft with reduced control effort,” *Nonlinear Dynamics*, Vol. 83, 2015. <https://doi.org/10.1007/s11071-015-2350-4>.
- [16] Shackcloth, B., and But Chart, R., “Synthesis of Model Reference Adaptive Systems by Liapunov’s Second Method,” *IFAC Proceedings Volumes*, Vol. 2, No. 2, 1965, pp. 145–152. [https://doi.org/https://doi.org/10.1016/S1474-6670\(17\)69028-1](https://doi.org/https://doi.org/10.1016/S1474-6670(17)69028-1), 2nd IFAC Symposium on the Theory of Self-Adaptive Control Systems, Teddington, UK, September 14-17, 1965.
- [17] Roman, S., *Advanced Linear Algebra*, Springer, 2008.
- [18] Zhang, F., *THE SCHUR COMPLEMENT AND ITS APPLICATIONS*, Springer, 2005.
- [19] Khalil, H. K., *Nonlinear Systems*, Prentice Hall, 2002.
- [20] Woodward, N., and Bevilacqua, R., “Onboard estimation of unknown dynamics of flexible spacecraft,” *Acta Astronautica*, Vol. 217, 2024, pp. 363–381. <https://doi.org/https://doi.org/10.1016/j.actaastro.2024.01.042>, URL <https://www.sciencedirect.com/science/article/pii/S009457652400050X>.
- [21] Hwang, J., “Attitude Stabilization of Spacecraft Using Moving Masses,” Ph.D. thesis, University of Texas at Arlington, 2016.
- [22] He, L., Sheng, T., Kumar, K. D., Zhao, Y., Ran, D., and Chen, X., “Attitude maneuver of a satellite using movable masses,” *Acta Astronautica*, Vol. 176, 2020, pp. 464–475. <https://doi.org/https://doi.org/10.1016/j.actaastro.2020.06.019>.
- [23] Wang, F., “Study on Center of Mass Calibration and K-band Ranging System Calibration of the GRACE Mission,” Ph.D. thesis, University of Texas at Austin, 2003.

- [24] Huang, Z., Li, S., Cai, L., Fan, D., and Huang, L., “Estimation of the Center of Mass of GRACE-Type Gravity Satellites,” *Remote Sensing*, Vol. 14, 2022, p. 4030. <https://doi.org/10.3390/rs14164030>.